University of Alberta

High Energy Proton Telescope

by

Fauzia Sadiq

A thesis submitted to the Faculty of Graduate Studies and Research in
partial fulfillment of the requirements for the degree of

Master of Science

in

Photonics and Plasmas

Department of Electrical and Computer Engineering

Dedicated

To
my husband, my parents and my brothers and sisters

who are a great assert of my life

Abstract

The Earth's magnetosphere is composed of energetic electrons and protons. It is important to verify average populations and energy distributions of these particles and quantify the effects of geomagnetic events on their populations and energy distributions. Abrupt changes have been observed in the energy and distribution of protons during magnetic storms creating a large population of very energetic (> 1 MeV) protons in the slot region of the Earth's Van Allen belts. A few attempts have been made in the past to investigate the sources and loss mechanism of these energetic particles. We have carried out detailed modelling of a High Energy Proton Telescope (HEPT) proposed as a scientific instrument for the proposed Canadian Outer Radiation Belt Injection, Transport, and Loss Satellite (ORBITALS) mission. HEPT is capable of measuring the energetic proton and electron distributions in the energy range of 3-120 MeV for protons and 3-20 MeV for electrons. The detector consists of two heads, one to cover the range of 3 to 26 MeV protons and the second to cover the range of 26 to 120 MeV protons with total view angles of 18° and 36°, respectively. The detector efficiency and geometric factors were calculated numerically using the GEANT4 high energy physics modelling code. In addition, model calculations were carried out to compare the model instrument performance with experimental measurements carried out at the TRIUMF accelerator facility giving good agreement. The results obtained indicate that the detector design would be suitable for a satellite mission to study energetic particle distributions during energetic solar particle events.

Acknowledgements

My first sincere gratitude goes to my Almighty Allah, His kind mercy made it possible to finish my Thesis.

It would not have been possible to write this thesis without the help and support of kind people around me.

I would like to express my deepest thanks to my supervisor Dr. Robert Fedosedjevs for his help, support, patience and guidance and providing me with an excellent atmosphere for doing research. I would like to thank my senior colleague Dr. Henry Tiedje for good advice and support.

I would like to thank my husband Asif for his personal support and great patience at all times. I would also like to mention my mother, grand mother, brothers and sisters who always pray for me.

I would like to appreciate valuable discussions and supporting environment from my friends and colleagues.

Table of Contents

List of Tables

List of Figures

List of Symbols and Abbreviations

ACRs	Anomalous Cosmic Rays
AE-8	Aerospace Corporation Electron version 8
AP-8	Aerospace Corporation Proton version 8
CERN	European Organization for Nuclear Research
CCD	Charged-Coupled Device
CME	Coronal Mass Ejections
CRAND	Cosmic Ray Albedo Neutron Decay
CGSM	Canadian Geospace Monitoring
CRRES	Combined Release and Radiation Effects Satellite
ELF	Extremely Low Frequency
FGM	Flux Gate Magnetometer
FOV	Field Of View
GTO	Geostationary Transfer Orbit
HEPT	High Energy Proton Telescope
HEH	High Energy Head
ILWS	International Living With a Star
ISTP	International Solar Terrestrial Physics
LEH	Low Energy Head
LWS	Living With a Star
MEO	Medium Earth Orbit
NIEL	Non-Ionising Energy Loss
ORBITALS	Outer Radiation Belt Injection, Transport and Loss Satellite
PROTEL	Proton Telescope on CRRES mission
SAMPEX	Solar Anomalous and Magnetospheric Particle Explorer

SSD	Silicon Solid-state Detectors
SSC	Storm Sudden Commencement
ULF	Ultra Low Frequency
VLF	Very Low Frequency

Chapter 1

Introduction

1.1 Introduction

After the discovery of radiation belts in 1958 it has become evident the radiation belts are a very important aspect of space weather that affects space missions. Thus for the past several decades, radiation belts have become an important subject of interest for the scientific and space communities [11]. The high energy proton and electron populations in the near-Earth space environment are some of the most significant hazards to the operation of satellites. These particles penetrate deeply into spacecraft and cause ionizing radiation damage to electronic and optical components as well as single event effects due to charge deposition in digital circuitry. Efforts have been made to measure and model the high energy protons in the Earth's radiation belts so that their effects on space systems can be better understood and predicted. Indeed average flux models such as AP8 and AE8 already exist and can be used as starting point for essassing radiation flux. However particle fluxes and energies are quite variable and more accurate monitoring is required to build a detailed data base for better models.
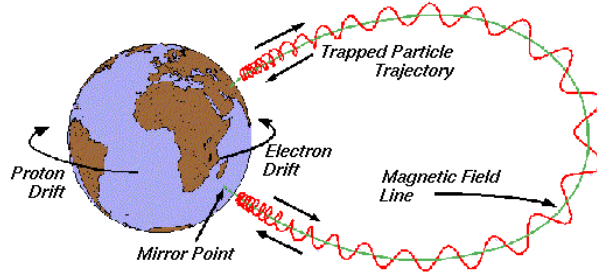
Figure 1.1: Figure illustrating three periodic movements of gyration, bounce and drift of charged particles in Earth's magnetic field. Figure reproduced from SPENVIS website [2]

1.1.1 Radiation Belt

Earth is surrounded by protons, ions and electrons forming torus shaped layers, called radiation belts. The local magnetic field of the Earth traps charged particles thus forming a protective layer around the Earth. It was found in 1958 that our Earth is surrounded by two radiation belts, the inner and the outer. Van Allen discovered the inner one while the outer one was discovered by S.N. Vernov and his colleagues [11].

Charged particles conduct three types of motions in the Earths magnetosphere (shown in Fig.1.1): gyration around the magnetic field lines, bounce motion along the magnetic field lines and drift motion across magnetic field lines as a result of the gradient and curvature of the magnetic field, forming toroidal trajectories centred on Earth's dipole centre called drift shells. Ions drift westward and electrons drift eastward also the higher energy particles drift faster than the lower energy particles [12].

Fig.1.2 shows a schematic of the radiation belts of Earth. It is divided into two layers. The inner belt is extended to 2.5 Earth radii and consists of energetic protons up to 600 MeV and electrons up to several MeV. The outer layer which can sometimes extend to 10 Earth radii mainly consists of electrons. The structure of inner belt is relatively stable in com-
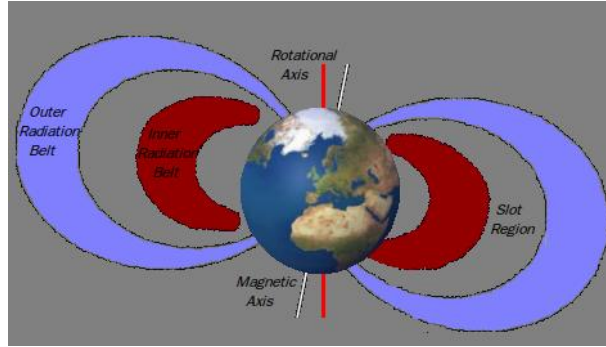
Figure 1.2: A schematic view of Van Allen Belts showing inner and outer layers. [3]

parison to the outer one, which is highly dynamic [13] and varies on the time scale of minutes, hours, months and years. There is a gap between the inner belt and outer belt, called the slot region, where normally a small number of particles can reside but it can be filled during active times.   In 1980s and 1990s a new belt called the Anomalous Cosmic Rays (ACRs) was discovered. The ACRs, so named because of its unusual ion composition and energy spectrum, consists of He, C, N, O, Ne, and Ar ions with an anomalous enhancement in the energy spectrum. The ACRs are formed by the neutral atoms in the interstaller space which penetrate into the heliosphere where they are ionized by solar UV radiation or by charge exchange with solar wind protons in the interplanetary medium [14]. These ionized particles are then coupled to solar wind and are carried outwards to the heliospheric boundary region where these accelerated particles then enter the orbit of the Earth after undergoing diffusion, convection and adiabtic deceleration. With the much improved time and spatial resolution of the Solar Anomalous and Magnetospheric Particle Explorer (SAMPEX) instrumentation, Cummings et. al. [4] measured the spatial distribution, the composition, and pitch angle distribution in great detail. It was found that the trapped ACR ions (He, O, N, Ne) are concentrated just south-east of the South Atlantic Anomaly with a sharp peak at L=2 in the energy range
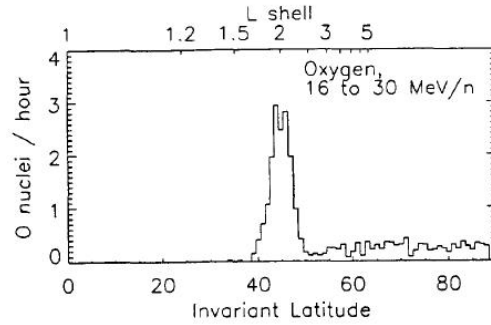
Figure 1.3: Measured ACR Oxygen ions versus L value. ©1993, IEEE [4]

of 16-50 MeV/nuclei where L is the McIlwain parameter [15] measured in Earth radii, and B/Bo (magnetic field strength normalized to its equatorial value on the field line). Fig.1.3 shows the concentration of Oxygen nuclei along L shell values.

The Sun is the main source and largest cause of change of radiation in space, although it is known that active acceleration processes also generate radiation around the Earth. The solar energetic particles are produced as a result of solar flares. A big solar flare results in a large amount of radiation around the Earth as the energetic particles from the Sun reach the Earth. To model the space environment it is very important to understand the cyclical activity of sun. The solar activity cycle is approximately 11 years long [16]. During this period there are typically 7 years when activity levels are high, the solar maximum, and 4 years during when activity levels are low, the solar minimum.

Although the number of sunspots is a common indicator of solar activity, the direct relation between the strength of the measured radiation events and number of sunspots is not straight forward. Events which emit a large number of solar particles are known to occur with greater frequency during the declining phase of the solar maximum. Trapped electron fluxes also tend to be higher during the declining phase [12].

4
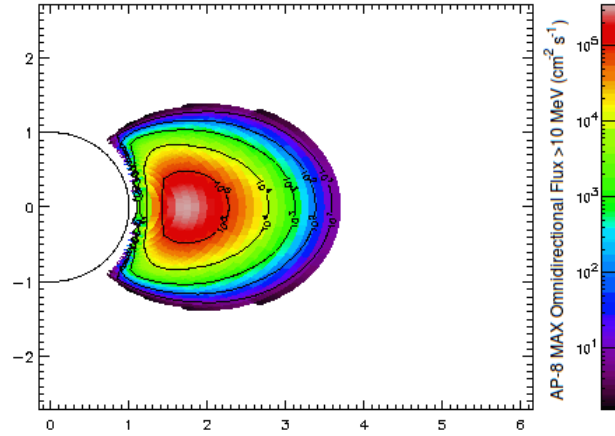
Figure 1.4: Invariant coordinate map of the AP-8 MAX integral proton flux > 10 MeV. The semi-circle represents the surface of the Earth and the distances are expressed in Earth radii (L shell values). Figure reproduced from SPENVIS website [2]
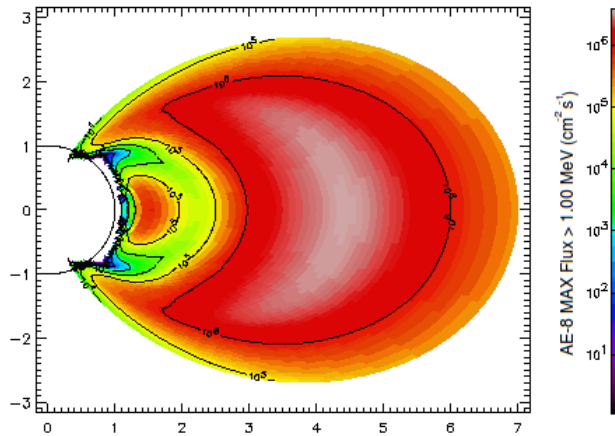
Figure 1.5: Invariant coordinate map of the AE-8 MAX integral electron flux > 1 MeV versus the L value. Figure reproduced from SPENVIS website [2]

As stated earlier, the radiation belts are linked to the existence of the Earth's magnetic field. The populations of particles are controlled by the sources and losses. The sources are the injection from the tail of the magnetosphere and creations by nuclear reactions between atoms in the upper atmosphere and energetic ions from solar or glactic cosmic particles. The losses take place by precipitation into the upper atmosphere or by charge exchange with the atoms and molecules from the exosphere. These processes depend greatly on the magnetic field and can vary over different time scales. Any major disturbance in the magnetic field results in a magnetic storm and variations of the fluxes in the radiation belt. Figs. (1.4) and (1.5) show the energy distribution function of protons and electrons in the radiation belt versus the L value.

Low energy protons ranging from some tens to some hundreds of keV are very sensitive to magnetic storms. At the beginning of each individual magnetic storm or substorm, protons are injected from the tail of the magnetosphere which increases the particle flux in the radiation belts. But at higher energy levels the belt is generally very stable and individual magnetic storms or substorms often do not affect those trapped particles. For the electron case it has been observed that low energy electrons respond very quickly after any disturbance in magnetic field while high energy electrons are detected few days after the event.

The High Energy Proton Telescope (HEPT) is one of the instruments which was to be included in a proposed Canadian satellite mission called the Outer Radiation Belt Injection, Transport and Loss Satellite (ORBITALS) mission [8]. This was proposed as a Canadian contribution to the International Living With a Star (ILWS) program [17]. ORBITALS was designed to be launched in a low inclination geostationary transfer orbit (GTO) with an apogee conjunction once per orbit with the Canadian

Geospace Monitoring (CGSM) array and the GOES East and West geosynchronous satellites. The ORBITALS mission was designed to measure electron and ion populations in the magnetosphere as well as dynamic electric and magnetic fields, waves and cold plasma to better understand the role of radiation belts in space weather in the near Earth environment. The specific goals of ORBITALS are detailed in the paper by Mann, et.al. [8]. The contribution of HEPT to the ORBITALS mission was the angularly resolved measurement of high energy protons and possibly also energetic light ions and electrons.

HEPT is capable of measuring the energy spectrum of protons in the energy range of 3 to 120 MeV with a 2D coverage once per satellite rotation. The HEPT design consists of two sensor heads, the Low Energy Head (LEH), intended for lower energy and High Energy Head (HEH) for higher energy protons. The HEH is also responsible to measure the energy spectrum of electrons ranging from 3 to 26 MeV. Each head contains a stack of silicon PIN detectors arranged in such a manner that measurements of proton energies is deduced from the signals of multiple detectors. This method is required to determine the direction of the proton as well as distinguish the protons from other particles, such as heavier ions or electrons. The average peak daily signal rated expected for the instrument are 21,500 and 650 protons per second for the low and high energy heads, respectively, which are estimated by taking the quiescent peak flux rates along the orbit of the satellite. The expected saturation flux rate for either head is expected to be in excess of 200,000 protons per second.

The project started in 2004 and an initial design was built with two PIN detectors which was tested at the University of Alberta in the Laser Plasma Research Laboratory with an alpha particle source. The final design of HEPT consists of eight PIN detectors with aluminum degraders.

A prototype with four detectors was tested at the TRIUMF beam facility. The first aluminum degrader and all the four detector elements had fixed thickness while by changing the thickness of the degrader elements on front and between the last two detector elements, different detector configurations of final HEH design were achieved.

The instrumentation and orbit of ORBITALS is similar to a previous science mission, the Combined Release and Radiation Effects Satellite (CR-RES) [18]. CRRES was flown in 1990-1991 and there has not been another science mission specifically to this region of space since. The PROTEL instrument on CRRES provided measurements of protons with energies between 1 and 100 MeV during the mission. Since the operation of HEPT is similar to PROTEL, the PROTEL design had been used as the starting basis when designing HEPT. The high energy head of HEPT will have a much higher count rate for various energy channels compared to PROTEL because of the factor of 4 times increase in geometric factor. To avoid saturation by high count rate events the low energy edge of the detector has been raised from 6 MeV in PROTEL to 26 MeV in the HEPT design.

1.2 Thesis outline

In the present study a High Energy Proton Telescope (HEPT) has been proposed and characterized. In the following chapters the design and analysis of the proposed detector is described. A brief outline of the thesis is listed below:

Chapter 2 of the thesis is intended to describe a brief theoretical background of radiation belts and previous space missions. The chapter includes a brief overview of the ORBITALS mission for which HEPT is designed. HEPT is based on energy deposited per unit length, also called dE/dx detector, so it is important to explain the physics of a dE/dx silicon

detector to understand the operation of HEPT. In order to estimate the space environment which will be probed various models of particle distributions and the expected fluxes for electron and proton based on AE-8, AP-8 models and CRRES data have been included. The acceptance angle and the geometric factor, which are important parameters of a telescope to give the efficiency of the device, will also be discussed briefly and compared to previous instrument designs in this chapter.

Chapter 3 discusses the Low energy detector head. Detailed design and modeling of LEH is described in this chapter. The detector response and energy deposition distribution of low energy protons is explained. The calculation of geometric factor for LEH is also included in this chapter.

The High Energy detector Head is designed to measure the proton energy ranging from 26MeV to 120 MeV and electrons with energy from 3MeV to 26 MeV. Chapter 4 discusses the detailed design and modeling of the HEH. Simulation are carries out to estimate the detector response and energy deposition in the Silicon detectors. A detailed geometric factor calculation for HEH is described in this chapter.

A four detector test design was used to test the operation of the HEH at TRIUMF test facility. In chapter 5 the design and modeling of this TRIUMF prototype detector is discussed. A comparison of the simulation data and test data is also described in this chapter.

In the last chapter of this thesis conclusions are presented. This chapter also contains some recommendations for future work.

Chapter 2

Theory and Background

2.1   Motivations

Significant progress in space techonology was made during the years following World War II. The field received a enormous boost during these years leading eventually to the great breakthrough of 1957 when Sputnik 1 beacame the first satellite to orbit the Earth in outer space. Many space missions have been sent now to explore the outer space environment and the solar system. Space technology has also served mankind. Many satellites have been sent to outer space which provide satillite navigation system, weather forecast, satellite television, radio and telephone services.

There are a number of processes which control the variable structure and dynamics of the radiation belts. The effects of these processes must be understood both singly and collectively in order to achieve dramatic improvements in space weather capability. The main challenge is that these processes act simultaneously, sometimes in the same region of space and sometimes in vastly different parts of the inner magnetosphere. The net effect of geomagnetic activity is determined by the state of the lower-energy source population and the magnetospheric transport processes including the effects of acceleration and loss. Furthermore, the whole chain of events takes place in a system of electric and magnetic fields that change dramatically in response to solar activity, solar wind energy inputs, the diamagnetic

effects of the ring current, substorms, ionospheric coupling and the whole host of interconnected parts of the Sun-Earth system [19].

Although significant efforts have been made in space science to understand the effects of solar and magnetospheric charged particles on biological and technological systems, there has been much less effort to study the effects of geomagnetic storms and magnetospheric substorms on space-based and ground-based communication, navigation and power distribution systems [20].

The inner magnetosphere is one of the regions of the magnetosphere which is poorly understood in detail. This region of geospace had not been extensively examined by the past space missions because of the harsh radiation environment and its deleterios effect on space instrumentation. Earths radiation belts are most strongly affected by the processes taking place in the inner magnetosphere. The processes of primary interests are acceleration and loss mechanism for energetic particles, the dynamics of the transient and extreme radiation belt structures, the effects of the ring currents and solar storm, and the controlling influences of the magnetospheric plasma environment, electric, and magnetic fields on the whole coupled system [8].

Due to their large energy range, trapped particles cause a variety of effects in spacecraft, components and biological systems. Low energy electrons contribute to spacecraft surface charging. High energy electrons injected and accelerated through the magnetotail can cause dielectric charge buildup deep inside geosynchronous spacecraft which may lead in turn to destructive arcing. Inner and outer belt electrons also contribute to ionising doses through direct energy deposition and bremsstrahlung effects. High energy protons (>10 MeV) in the inner radiation belt are the main contributors to ionising dose deposition in shielded components, where cosmic

rays and solar energetic particles are effectively shielded by the geomagnetic field. Lower energy protons (up to 10 MeV) contribute to Non-Ionising Energy Loss (NIEL) dose which affects Charged-Coupled Devices (CCD) and other detectors. Unshielded detectors can be affected even in the outer belt, where protons with energies < 1 MeV are present [2]. Non ionising energy is the energy a particle transfers to a solid without ionising it. Particles hitting solid state material can displace the atoms of the material causing a displacement damage which reduces the charge transfer efficiency of the material.

2.2   Theoretical Background

With the discovery of the radiation belts it was realized by space scientists that it was important to understand the radiation environment in which satellites would operate. Many measurements were done in 1960's and 1970's to develop models on the near-Earth radiation environment. The early models provide very useful first order understanding of radiation hazards in the near Earth space environment. But there were limitations on the number of measurements which could be made and the capability of the instrumentation. However over the time the technology has become more sophisticated allowing for better measurements to be made. Since the high energy proton, electrons and ions in the Earth space environment pose significant hazards to the operation of satellites, a better knowledge of space environment not only can increase the average lifetime of spacecraft but also can help to develop better methods to protect the crew from radiation effects. Therefore, it is important to upgrade the radiation belt models to meet the accuracy needed for today's space systems [21].

Since the early 1970's continuous improvements have been made to the radiation belt models by adding new data sets, extending the energy

ranges, etc. The latest versions of electron and proton models developed by NASA are called AE8 and AP8, respectively. They are provided by the NASA and are much improved over the initial models, but still have deficiencies which are becoming more apparent due to new miniaturized electronics in the spacecraft [18].

By realising the need of cooperation between different nations, NASA proposed Living With a Star (LWS) program in fall 2000. International Living With a Star is an international cooeperative program in solar terrestrial physics established by the major space agencies of the world (USA, Japan, Russia and European Countries). The program is a follow on of the International Solar Terrestrial Physics (ISTP) program. the main objectives of the program are to stimulate, strengthen, and coordinate space research to understand the processes that are responsible to connect the Sun-Earth System. The scientific goals of ILWS include future solar, heliospheric and solar terrestrial missions which are important in both applied and fundamental sciences [17]. The outer radiation belt injection, transport, acceleration and loss satellite (ORBITALS) is also a small satellite mission proposed as a Canadian contribution to the satellite infrastructure for the ILWS program.

ORBITALS would monitor the energetic electron and ion populations in the inner magnetosphere across a wide range of energies as well as the dynamic electric and magnetic fields, waves and cold plasma environment which govern the injection, transport, acceleration and loss of these energetic and space weather critical particle populations [8]. The High Energy Proton Telescope (HEPT) is one of the instruments planned for the ORBITALS mission to measure the energy spectrum of electrons and protons.

2.2.1 Past work

The study of space in the period 1958 and 1978 established the average fluxes and energies of the electrons and protons trapped in the Earth's radiation belts. On the basis of these studies different empirical models have been derived which gave a general but static view of the radiation belts. A series of models for protons and electrons was developed by NASA. The models are based on data from more than 20 satellites from the early sixties to the mid-seventies. AP-8 (Aerospace Corporation Proton version 8) and AE-8 (Aerospace Corporation Electron version 8) are the latest editions in a series of updates starting with AE-1 and AP-1 in 1966, give proton and electron spectra at the solar minimum and maximum. These models contain omnidirectional, integral electron (AE maps) and proton (AP maps) fluxes in the energy range 0.04 MeV to 7 MeV for electrons and 0.1 MeV to 400 MeV for protons in the Earth's radiation belt (L = 1.2 to 11 for electrons, L = 1.17 to 7 for protons). The fluxes are stored as functions of energy, L-value [21]. Figs. 2.1, 2.2, 2.3 and 2.4 show the integral flux for solar minimum and maximum for protons and electrons taken from the AP-8 and AE-8 models for a defined orbit with perigee and apogee of 6630 km and 33,850 km, respectively.

The CRRES mission was dedicated to determine the structure and dynamics of the radiation belts using more modern detection instruments. One of the important objectives of CRRES was to assess the effects of trapped radiation on electronic components in space. During 25 July 1990 to 22 March 1991 data of CRRES showed that there was primarily a single inner zone proton belt around L= 1.6 and these trapped protons produced a strongly peaked spatial occurrence of spacecraft interactions. After a strong geomagnetic storm on 24 March 1991, the inner zone belt structure changed extending to larger L values and forming a second peak around
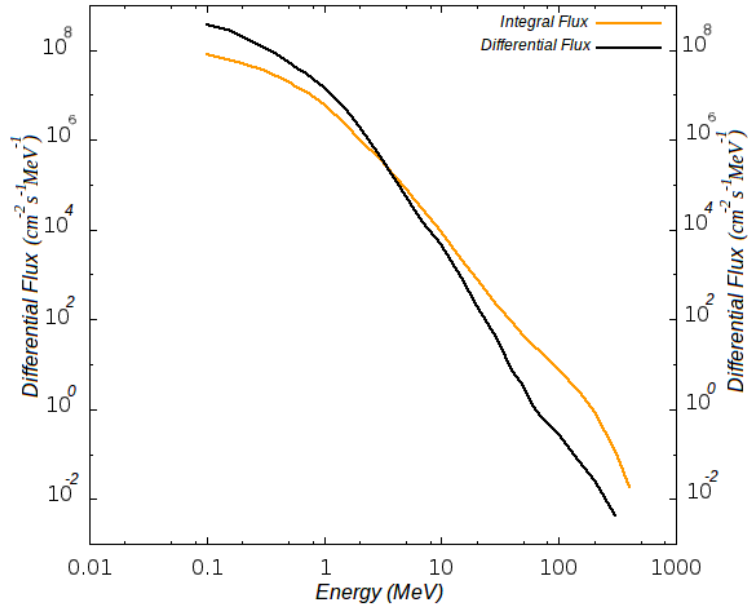
Figure 2.1: Integral flux $(cm^{-2}s^{-1})$ and differential flux $cm^{-2}s^{-1}MeV^{-1}$ versuss Energy from AP-8(MIN). [5]
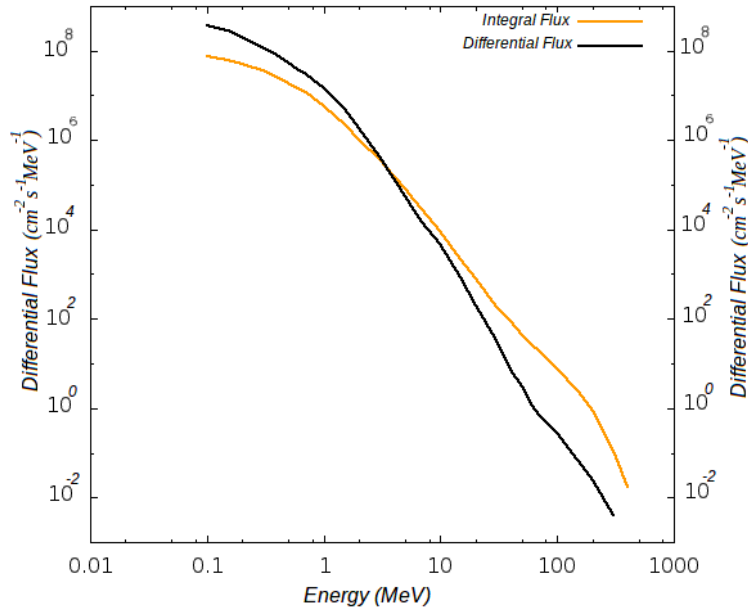
Figure 2.2: Integral flux $(cm^{-2}s^{-1})$ and differential flux $cm^{-2}s^{-1}MeV^{-1}$ versus Energy from AP-8(MAX). [5]
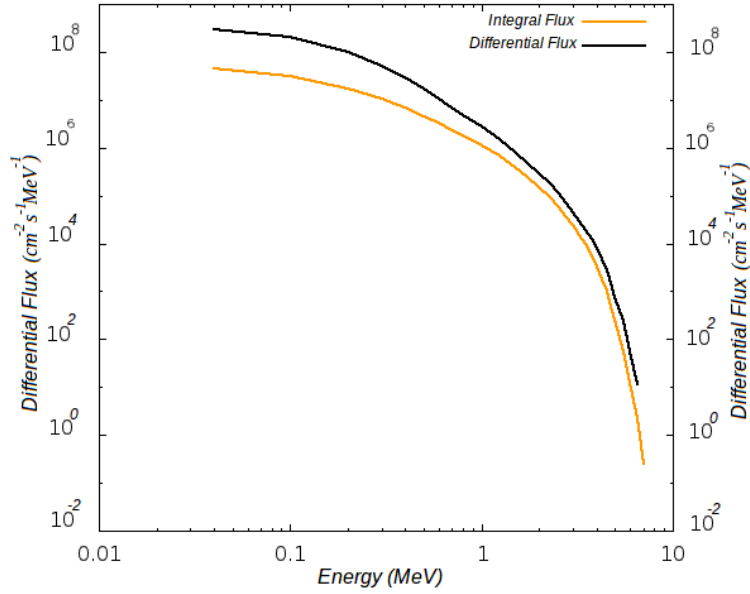
Figure 2.3: Integral flux $(cm^{-2}s^{-1})$ and differential flux $cm^{-2}s^{-1}MeV^{-1}$ versus Energy from AE-8(MIN). [6]
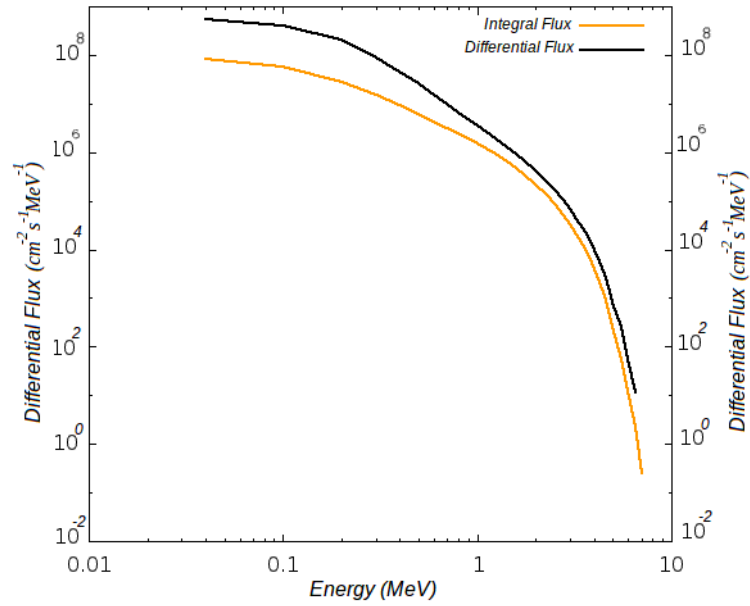
Figure 2.4: Integral flux $(cm^{-2}s^{-1})$ and differential flux $(cm^{-2}s^{-1}MeV^{-1})$ versus Energy from AE-8(MAX). [6]
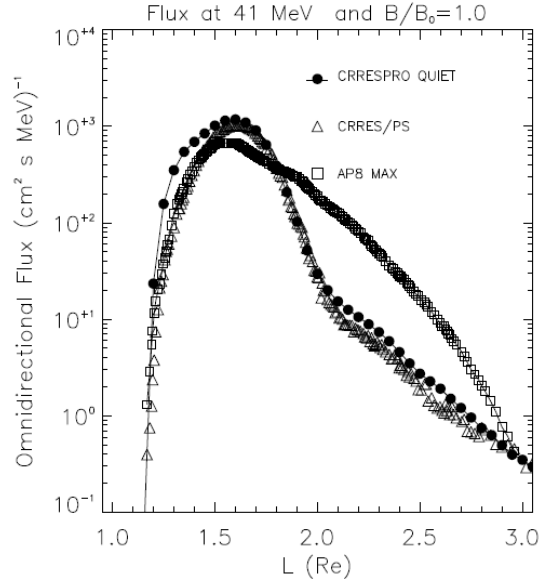
Figure 2.5: Omnidirectional flux during quite time. Reprinted with permission of the American Institute of Aeronautics and Astronautics [7].

L=2.3 [20]. CRRES-PRO and CRRES-ELE are the models for protons and electrons based on CRRES data. Figs.2.6 and 2.5 show omnidirectional flux of protons during quiet and active times as predicted by CRRESPRO, CRRES P/S and AP-8 models. CRRESPRO and CRRES P/S are the models based on observations of PROTEL and proton switches (PS) respectively. Both were proton energy detectors flown on CRRES [7].

Observations by geosynchronous satellites, by CRRES, SAMPEX mission and POLAR have now shown that the radiation belts are highly structured and highly dynamic exhibiting variability on time scales of minutes, days, seasons, and the solar cycle [22]. Table 2.1 lists brief information about these space missions. The fluxes of radiation belt electrons and ions vary in response to solar wind conditions and in response to geomagnetic storms but those variations are poorly understood and unpredictable. Usually an increase of the fluxes of radiation belt electrons and ions are observed during high-speed solar wind driven storms, a given storm might
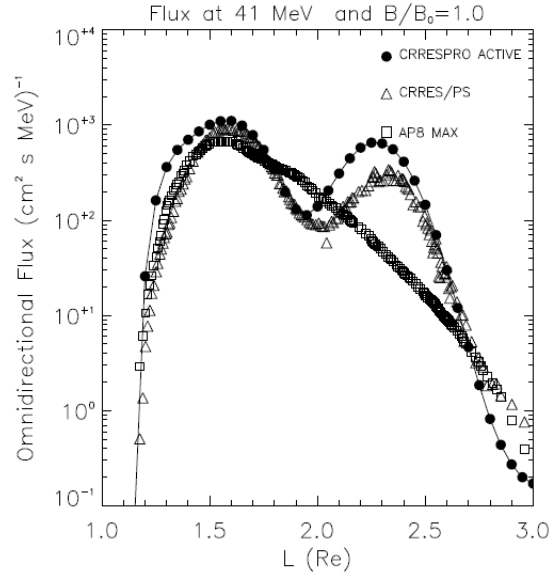
Figure 2.6: Omnidirectional flux during active time. Reprinted with permission of the American Institute of Aeronautics and Astronautics [7].

Mission	Period (hrs)	Orbit(km)	Inclination	Year
CRRES	10	350/33,500 [23]	18.1^0	1991
SAMPEX		550/675 [24]	82^0	1992
POLAR	22.6	11500/57000 [25]	86^0	1996

Table 2.1: Some space missions of the past and their important parameters.

either decrease radiation belt fluxes if it had been increased by a previous storm. The reason is still unknown, which reflects the fact that the processes that transport, accelerate, or remove particles from the system are still unpredictable [19].

The inner part of the proton radiation belt, L < 2.0, is very stable, while in the outer part of radiation belt, L > 2, dramatic variations have been observed, especially during solar storms and strong interplanetary shocks. For example, during the storm sudden commencement (SSC)

recorded on March 24, 1991 by CRRES mission, a new proton belt was formed within just 3 minutes [20]. Sometimes the magnetosphere is compressed by an abrupt enhancement of the solar wind dynamic pressure prior to the main phase of a storm. This is called SSC, which is followed by a storm's initial phase. It is thought that the Cosmic Ray Albedo Neutron Decay (CRAND) is mainly responsible for quiescent protons with energies > 100 MeV. Solar protons from solar events are the main source of protons in the radiation belts. The inward transportation of protons by radial diffusion is important for their acceleration. The dominant causes of loss of protons are Coulomb collisions with thermal plasma in the plasmasphere and atmospheric absorption. The precipitation into the ionosphere due to the pitch angle scattering is also important.

Theoretical and observational studies of energetic electron losses have been carried out since the late 1960s. Observed decreases in the trapped flux can be caused by adiabatic effects, or real losses through either precipitation into the atmosphere or magnetopause shadowing. In the inner belt, the electron flux is usually stable, while the electron flux sometimes increases in association with large magnetic storms. During the strong SSC event on March 24, 1991, injection of tens of MeV electrons was observed at L = 2 [20]. Electron flux variations in the radiation belts are the result of achieving a balance between source, transport and acceleration, and loss processes [26]. Different processes for acceleration/transportation and loss occur simultaneously during storms.

Space Weather has become an important issue for space and Earth applications since the effect Solar Wind and particularly large Coronal Mass Ejections can have on large adverse effects on many of these applications. Monitoring Solar Activity and coronal mass ejections (CMEs), and forecasting these events by using different spacecraft has become common practice,

but forecasting the response of Geospace is nearly impossible with the current level of understanding of the physical processes that are responsible for these responses. Understanding these processes is an important step to improving forecasting models.

2.3   ORBITALS Mission

The outer radiation belt injection, transport, acceleration and loss satellite (ORBITALS) is a small satellite mission proposed as a Canadian contribution to the satellite infrastructure for the International Living With a Star (ILWS) program. The main purpose of ORBITALS was to monitor the energetic electron and ion populations in the inner magnetosphere across a wide range of energies (from keV to 10-100 MeV) as well as the dynamic electric and magnetic fields, waves and cold plasma environment which govern the injection, transport, acceleration and loss of these energetic and space weather critical particle populations [8].

2.3.1   Design

The ORBITALS was designed as a hexagonal small satellite bus sun-aligned spin-stabilized spacecraft, with a nominal spin period of around 10 s. Thus a single look direction telescope could measure 2D pitch angle distributions in a plane containing the nominal background magnetic field once per spin. For instruments with 2D coverage, full 3D particle distribution functions can be produced once per spin. The spacecraft body was designed to be made up of a honeycomb structure aluminium shell providing shielding equivalent to 4 mm of aluminium shielding along with an additional shielding of aluminum copper and tungsten for the components and instrument boxes inside the outer housing. The ORBITALS science payload was proposed to be comprised of 7 instruments for monitoring the
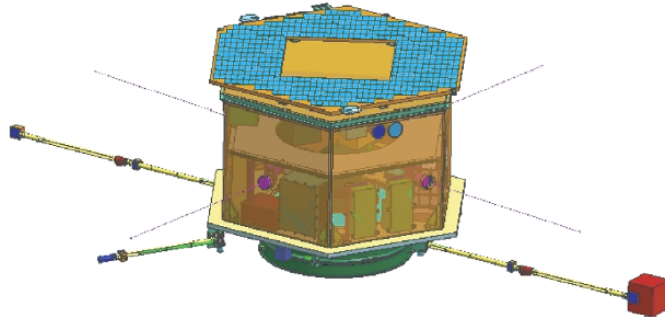
Figure 2.7: ORBITALS mission [8]

energetic inner magnetosphere particle populations, the background electric and magnetic fields, and the extremely low frequency (ELF), very low frequency (VLF) and ultra low frequency (ULF) waves [8].

2.3.2 Mission Objectives and Goals

The main objectives of ORBITALS mission were to study the dynamical variation of outer radiation belt electron flux, inner radiation belt electron and ion fluxes and to determine the dominant acceleration and loss processes. To investigate the structure of global inner magnetospheric electric and magnetic fields, core ion composition of the outer plasmasphere, plasmapause and plasmatrough regions and its dynamics during storms was also an important task of the ORBITALS mission. Another important objective was the study of dynamical behavior of the strength, asymmetry, composition and energization of the ring current in the inner magnetosphere. The mission also included the study of nightside near-Earth plasmasheet flows and instabilities.

Thus the primary goal of the ORBITALS mission was to determine the dominant processes responsible for the acceleration, losses, global distribution and variability of energetic electrons and ions in the inner magnetosphere. As stated earlier because of various wave particle interactions very important coupling exists between particles of widely differing ener-

gies. Realizing this, a significant goal of the ORBITALS mission was to focus specifically on understanding the pathways for particle-wave-particle energy transfer which could affect MeV energy radiation belt particle dynamics and radiation belt structure. Furthermore, ORBITALS was to provide important monitoring of electrons and ions from the inner belt through Medium Earth Orbit (MEO) to close to geosynchronous orbit at energies (from keV to 10-100 MeV) which are important for space weather satellite charging. These measurements could be used as inputs for the development of the next generation of radiation belt specification models to replace AP-8 and AE-8 etc.

2.3.3 Orbit of ORBITALS

The ORBITALS orbit was designed to traverse from the inner belt at low inclination to measure maximum extent of particle distribution trapped in the mirror fields, through the slot region and across the outer belt, to close to geosynchronous (GEO) orbit. With the careful orbit selection, it would be possible to maximize the magnetic conjunctions to the extensive ground-based instrumentation in the Canadian Geospace Monitoring (CGSM) program as well as to other US operated ground-based instrumentation in this sector.The orbit also had apogee to provide conjunctions close to the GOES East and West and other commercial spacecraft which operate at geostationary orbit (GEO) in the North American sector.

In order to meet the required mission goals, two orbits with different perigees were considered. The first, ORBIT A (baseline orbit), was designed with a 12 h orbital period, geocentric perigee of 13,011 km (inner radiation belt, 2.04 R_E) and an apogee 40,139 km (outer radiation belt,6.3 R_E). There also exists an alternative orbit, ORBIT B, with perigee around 560 km and with a range of apogee heights slightly above or below the

apogee altitude of ORBIT A. These orbits would have period shorter than 12h.

As described earlier HEPT was one of the science payloads with two solid state telescopes providing 2D, 3-100 MeV energetic ion coverage once per spin. The HEH of HEPT was to study the very high energy inner belt protons and electrons in the inner and outer belts. The performance specifications of PROTEL and the HEPT detectors are compared in Table 2.2

By comparing the design of HEPT and PROTEL, it can be seen that the proposed design of HEPT weighs larger than the PROTEL and was supposed to consume about the same power of PROTEL. HEPT has a larger geometric factor with a similar angular resolution, defined by the full viewing angle, and a slightly higher specification on the lowest energy of protons that will be measured when compared to PROTEL. The differences are subtle but depend mostly on the energy ranges selected for the detector heads. The PROTEL low energy head was dominated by protons with energies less than 3 MeV, the absence of which will allow HEPT to measure a higher dynamic range of particle fluxes in the 3-26 MeV range with better statistical accuracy due to the larger geometric factor.

A large performance enhancement will come from the fact that the electronics for the HEPT high energy head are being designed to complete the measurements of proton energies within $1\mu s$, whereas the equivalent PROTEL dead time between measurements was 2 μs. The significance of this increased measurement speed was important for the measurement of the proton populations before, during and after magnetic storm events.

	HEPT University of Alberta Current		PROTEL Air Force Geophysics Laboratory 1990-1991	
Satellite rotation period (sec)	10		30	
Proton Binning Angular Resolution	12° (1/2 second intervals)		12° (1/2 second intervals)	
Perigee/Apogee (*km*)	6630/33,850		350/33,500	
L value	2.04-6.2		1.1 - 4	
Mass	18.75		17.25 kg	
Power Consumption (W)	15.5 W		14 W	
	Low Energy Head	High Energy Head	Low Energy Head	High Energy Head
Energy Range (MeV)	3-26	27 -120	1-9	6-100
Full Viewing Angle	18°	24°	19.3^o	33.8^o
Geometric Factor	0.030	0.565	0.012	0.119
Energy Detectors	5	10	4	5
Coincidence Detectors	5	10		
Maximum counting Rate	200,000 cps	200,000 cps	255,000 cps	255,000 cps [27]

Table 2.2: Comparison of HEPT form ORBITALS and PROTEL from CRRES.

The increase in populations of high energy protons during storms can be as much as three orders of magnitude higher than quiescent and a large dynamic range is required to properly measure these phenomena. These population fluctuations occur on time scales on the order of 10 seconds which matches the rotational period of the ORBITALS well.

2.4 Particle Identification

Particle identification is an important factor in space physics. The particles interact with matter in different ways, thus offering different possibilities to build detectors. In order to detect either charged or neutral particles in space, few types of detectors are used. These include Faraday cup devices to measure the current associated with charged particle distributions, windowless electron multipliers such as channel electron multipliers (Channeltrons) and microchannel plates that may be operated in either a pulse counting or an integrated current mode, and solid-state or scintillation detectors used for higher energy particles [28].

2.4.1 Ionisation energy losses

Ionisation energy losses play important role to detect charged particles. Here the quantity to be measured is the average amount of energy lost per unit length of distance travelled, dE/dx, which is also called the stopping power. This was calculated by Bohr for the classical case and by Bethe Bloch and others by using quantum mechanics.

2.4.2 Solid State Detectors

Silicon solid-state detectors (SSD) are built using ultra pure silicon crystals. They are manufactured in several types, depending on the dopants introduced to the crystal and the method by which they are introduced into

the crystal lattice. However, the basic operation of all the types of detectors is the same. As a charged particle traverses the crystal it interacts with the valence band electrons and promotes them to the conduction band. Once in the conduction band, electrons are free to move in response to an externally applied electric field. For each electron promoted, a hole is created in the valence band. The hole behaves as a positively charged particle and also moves in response to the electric field. Both electrons and holes are referred to as carriers. As the secondary conduction band electrons move through the crystal, they also interact with the valence electrons and create more electron-hole pairs. At the end of this cascade process approximately 3.6 eV are required to produce one electron-hole pair in silicon. Crystals typically will have electrodes on both sides and operate as a reverse biased diode. The applied electric field attracts the carriers to their respective electrodes and prevents them from recombining. Total charge collected at the electrode is proportional to the energy lost in the crystal by the incident particle. If the incident particle is completely stopped in the crystal the collected charge is proportional to the total particle energy.

In order to understand the response of sensors to high energy particles the process of energy loss of particles in matter plays an important role. Heavy charged particles, such as protons, interact with the material as a result of series of collision with the electrons while traversing the material. A small amount of energy is lost as a result of each interaction. As the mass of proton is greater than that of electron the scattering of the proton is almost negligble. The result is that protons travel in nearly straight lines. Electrons, on the other hand, can lose a large fraction of their energy and undergo significant angular scattering in a single collision with a target material electron since both particles have the same mass. In addition, the electron direction of motion can also be changed greatly

by a collision with an atomic nucleus. The energy loss process of heavy charged particles, (protons and other ions) is thus different from light particles (electrons). The stopping power, dE/dx, for heavy particles is given by the Bethe-Bloch formula [29]

$$-\frac{dE}{dx} = \frac{4\pi N_A z^2 e^4}{m_e c^2 \beta^2} B \qquad (2.1)$$

where

$$B = \frac{Z\rho}{A}\left[ln\left(\frac{2m_e c^2 \beta^2}{I(1-\beta^2)}\right) - \beta^2 - \frac{C}{Z} - \frac{\Delta}{2}\right] \qquad (2.2)$$

where x is the path length, N_A is Avogadros number, z is the charge of the incident ion, m_e is the electron rest mass, e is the electronic charge, c is the speed of light in vacuum, β is v/c for the proton, Z, ρ and A are the atomic number, mass density and atomic weight of the stopping material and I is the averaged excitation potential per electron in the target. The density correction Δ only becomes important at high energies (when the kinetic energy of the particle exceeds its rest mass for example for proton it is > 938 MeV) and shell correction C is important at low energies (1-100 MeV with a maximum correction of about 6%.) [29]. A list of the relevant I , C and Δ parameters for all elements can be found in Janni [30]. For non-relativistic particles, $v << c$, only the first term in equation (2.2) is significant, the third term also contributes if the particles have low energies. Equation (2.1) is generally valid for ions with velocities greater than those of atomic electrons. Since the B term varies slowly with energy, the energy loss varies inversely with energy [13]. As a particle velocity decreases from relativistic energies, the particle-electron collisions need to be considered with detailed evaluation of each target electrons orbital bonding in order to obtain accurate stopping powers.

In case of thin absorbers, the energy loss in the material, ΔE, is given by

$$\Delta E = -\frac{dE}{dx}t \qquad (2.3)$$

27

where t is the absorber thickness. For cases where the thin absorber approximation cannot be applied, the energy loss ΔE is obtained by integration of equation (2.1) over the detector thickness.

Angular scattering can also be important in the case of interactions of ions and absorber, which alters the direction of motion ion without affecting its energy significantly. Angular scattering may play an important role in instruments that use multi-element telescopes. In this case angular scattering in the upstream detectors may prevent some particles from being detected. This will result in an underestimate of the true incident particle fluxes. The angular scattering for ions is given by [13]

$$< \theta^2 > = \frac{\pi N Z_1 (Z_1 + 1) Z_2^2 e^4}{E^2} ln \left(\frac{4\pi N a_0^2}{Z_1^{2/3} + Z_2^{2/3}} \frac{Z_1 + 1}{Z_1} \right) \qquad (2.4)$$

where θ is the scattering angle in radians, Z_2 is the nuclear charge of the incident ion, Z_1 is the nuclear charge of the target material atoms, N is the areal density of the target atoms, E is the incident particle energy, e is the electronic charge and a_0 is the Bohr radius. Equation (2.4) is valid for protons with energies above a few MeV.

The process of energy loss by electrons is much more complex than for ions due to the electrons small rest mass. Electrons are scattered significantly in materials, some times enough to scatter them back out of the material. The backscattering of electrons depends on the Z of the material and increases with increase in Z. The emission of Bremsstrahlung or electromagnetic radiation is another factor in the electron stopping power. Bremsstrahlung is emitted whenever the electron is accelerated, such as when it is deflected through a large angle or undergoes a collision with a large energy loss. Thus part of the energy loss is radiated away as Bremsstrahlung x-rays and this would not be detected by a silicon detector since the absorption cross-section for x-rays is much less than for the

initial electrons. However the fraction of loss is small for electron energies of the order of a few MeV.

2.5 GEANT4 Modeling

A simulation model allows one to examine system behavior under different scenarios in virtual computational world. It provides a safe, and relatively cheap testbed to optimize the performance and to evaluate the side effects of the system before implementing the design in the real world. With the use of advanced detector techonology in particle and nuclear physics experiments it has become more challenging to create robust software frameworks and applications for such type of experiments. GEANT4 is a toolkit used to simulate particles passing through and interacting with matter acurately. The free software package includes all the processes e.g. geometry, material, tracking, physics processes which govern particle interactions, visulisations, etc. One can use the built-in routine interface or define user interface according to one's requirements [31].

In 1993 it was proposed by European Organization for Nuclear Research (CERN) and High Energy Accelerator Research Organization (Japan) known as KEK to develop the existing GEANT3 program [32] which was in FORTRAN into a new toolkit by writing it in C++, to meet more advance requirements. GEANT4 is the resiltant object-oriented toolkit which provides comprehensive detector and physics modeling capabilities. The core of GEANT4 is a set of physics models to handle the interactions of particles with matter across a very wide energy range. The GEANT4 Collaboration takes care of its development maintenance and provides documentation and user support. Documentation includes installation, user and reference guides, and a range of training kits. It is intended to cover the need of the beginner through to the expert user who wishes to

expand the capabilities of GEANT4 [31].

The physics results are made transparent by exploiting Object Oriented Technology in GEANT4 physics processes. For example the final state of a process can be computed by the energy range, the particle type, the material. GEANT4 provides a number of processes in which a particle interact with matter e.g. electromagnetic, hadronic, decay, optical process etc. The electromagnetic physics manages lepton (electron, muon) physics, gamma, x-ray and optical photon physics. The hadronic physics offers both a data and a variety of theory driven models for physics beyond test-beams energies, as well as treating low energy neutron transport. The Run, Event and Track management allows the simulation of the event kinematics, together with primary and secondary tracks. Visualisation and User Interface allows to interact with sophisticated GUIs or command line and batch systems.

Since GEANT4 toolkit provides both full and fast MonteCarlo simulation of detectors. It has great uses in High Energy Physics. It is designed to take into account also the requirements of space and cosmic ray applications, nuclear and radiation computations, heavy ion and medical applications.

2.6   Distribution Function for Isotropic Source

As the proportionality constant or geometric factor is valid only for an isotropic flux it is easiest to calculate when an isotropic source is used. In order to demonstrate that the GEANT4 source is itself iostropic the distribution function was checked and it was shown that the flux produced by the source used was isotropic. To calculate this distribution function an isotropic source of radius 1 mm was placed 21 cm away from a flat detector array with an axial angle θ between 0^0 to 30^0 and azimuthal angle, ϕ,
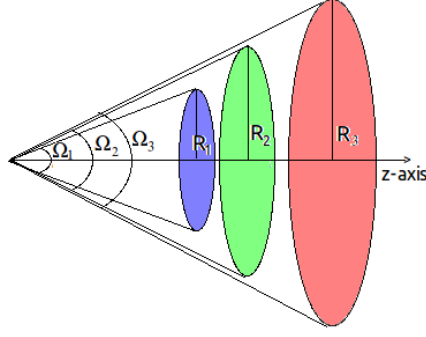
Figure 2.8: Isotropic source and array of detectors with increasing solid angle for each disk. All detectors are located at the distance l=21 cm from the source but they are displaced axially on this figure for clarity.

randomly chosen in the range from 0^0 to 360^0 (a solid angle of cone angle of 0.8415 steradians). An array of detector disks with increasing diameters from 2 cm to 26 cm with 1 cm increase in diameter fom one disk to the next was placed on axis as shown in Fig.2.8. Each detector was placed 21 cm apart from the source i.e l=21 cm one by one. The total number of events used were 100,000 for each run. The distance between the source and the detector edge varies with increasing radius as $r = \sqrt{l^2 + R^2}$, where R is the radius and l is the distance of the detectors from the source.

Since the source is very small as compared to its distance from the detector it can be taken as a point source. As the diameter of the detectors increased with radius so does the total solid angle of each detector seen from the source as shown in Fig.2.9. The solid angle subtended by a disk of radius R can be calculated as:

$$\Omega = 2\pi(1 - \frac{l}{\sqrt{l^2 + R^2}}) \tag{2.5}$$

For small values of θ, it can also be calculated as:

$$\Omega = \pi sin^2\theta \tag{2.6}$$

The source was made to emit particles over a limited solid angle range for
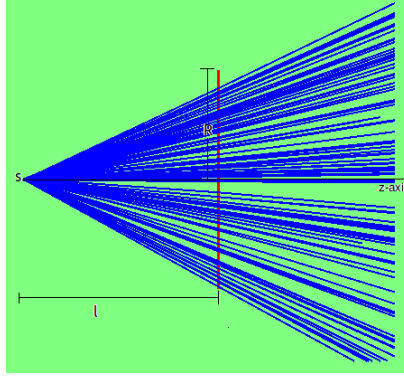
Figure 2.9: Isotropic source with limited axial angle.

θ from 0^0 to 30^0 and ϕ from $0 - 2\pi$, so the total solid angle subtended by a disk shaped detector which covers the whole beam is given by

$$\Omega = 2\pi(1 - cos30) = 0.8415 srad \qquad (2.7)$$

The solid angle for each detector ring with increasing value of radius R is given by

$$\Delta\Omega = 2\pi\left(\frac{l}{\sqrt{l^2 + R_2^2}} - \frac{l}{\sqrt{l^2 + R_1^2}}\right) \qquad (2.8)$$

where R_1 and R_2 are the radii of detector rings 1 and 2, respectively. It should be noted that each detector has same distance l from the source and they are replaced one by one for each run.

Table 2.3 lists the flux observed (F_{obs}) by the simulation, the expected flux (F_{exp}) and the solid angle of each detector. The number of particles hitting the detector of radius R observed by simulations and the expected number of particles versus radius of the detector are plotted in Fig. 2.11. It can be seen that the observed number is in good agreement with the expected flux for each ring detector of radius R. The flux per steradian for an isotropic source is a constant quantity. Therefore, it is expected that the change in flux per steradian of solid angle should be the same for all detectors and the plot of flux per steradians vs R should be a constant line. The expected flux per steradian and the observed flux per

R	$\Omega(srad)$	$F_{observed}$	$F_{observed}/\Omega$	$F_{expected}$
1	0.0071	836	117612	844
1.5	0.0160	1812	113538	1896
2	0.0283	3200	113120	3360
2.5	0.044	4990	113322	5231
3	0.0631	7186	113851	7498
3.5	0.0854	9848	115253	10151
4	0.1109	12643	113989	13176
4.5	0.1394	15918	114188	16561
5	0.1708	19551	114482	20288
5.5	0.2049	23351	113961	24342
6	0.2416	27567	114087	28705
6.5	0.2808	32329	115130	33359
7	0.3223	37025	114888	38285
7.5	0.3659	41914	114563	43464
8	0.4114	47420	115260	48876
8.5	0.4588	52699	114869	54502
9	0.5078	58435	115082	60322
9.5	0.5582	63955	114565	66319
10	0.61	70100	114911	72472
10.5	0.663	76165	114880	78764
11	0.717	82668	115300	85177
11.5	0.7718	88837	115098	91694
12	0.8276	95275	115145	98299

Table 2.3: Observed flux and the expectected flux for each detector ring of outer radius R
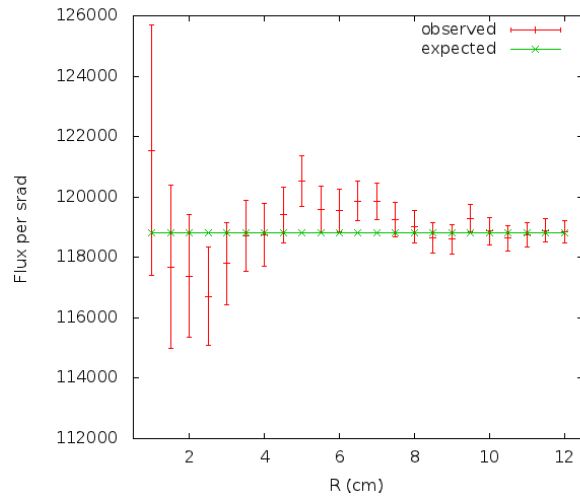
Figure 2.10: Plot of the flux per srad observed by simulation and that expected for an isotropic source for each disk of radius R.
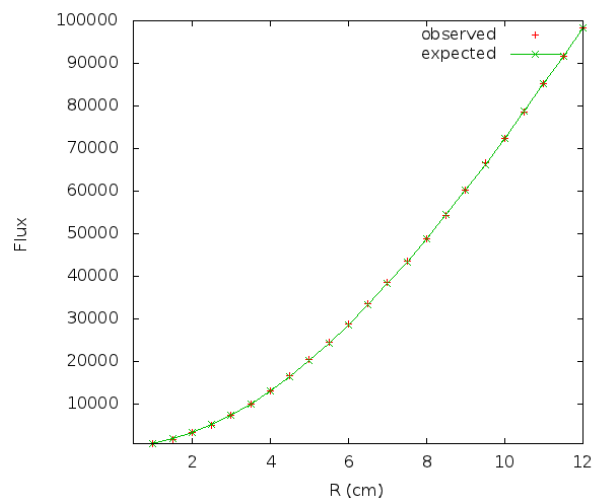
Figure 2.11: Plot of the observed flux obtained by simulation and that expected for an isotropic source for each detector ring vs radius R.

R	ΔF_{obs}	$\Delta\Omega$	$\Delta F_{obs}/\Delta\Omega$
1	976	0.009	109663
1.5	1388	0.012	112846
2	1790	0.016	114013
2.5	2196	0.019	114974
3	2662	0.022	119372
3.5	2795	0.026	109608
4	3275	0.029	114912
4.5	3633	0.031	115701
5	3800	0.034	111437
5.5	4216	0.037	114877
6	4762	0.039	121480
6.5	4696	0.042	113157
7	4889	0.044	112133
7.5	5506	0.046	121011
8	5279	0.047	111371
8.5	5736	0.049	117061
9	5520	0.050	109524
9.5	6145	0.052	118629
10	6065	0.053	114434
10.5	6503	0.054	120426
1 1	6169	0.055	112573
11.5	6438	0.056	115791

Table 2.4: Incremental change in flux ΔF for each additional axial ring and solid angle $\Delta\Omega$ for each axial ring.

steradiansby simulations are plotted versus radius of the detector in Fig. 2.10. Fig. 2.10 shows that the observed flux per steradians with respect to R is in agreement with the expected flux which indicates that the source is indeed isotropic.

2.7   Geometric Factor

A particle telescope consists of an entrance aperture, which allows particles to enter, a shielded body and detector elements. Often semiconductor detectors are used as sensors to measure the energy of the particles. The number of particles can be characterized and counted as they pass through the telescope. The particle flux can be calculated from the number of counts per unit time and acceptance aperture of the detector. The counting rate of any particle telescope depends upon the effective dimensions and relative positions of the sensors, the intensity of radiation in the surrounding space and the detection efficiency of the sensors. For an ideal telescope, the factor of proportionality relating the counting rate to the particle flux intensity is defined as the gathering power of the telescope. When the intensity is isotropic, the factor of proportionality is called the geometrical factor. The geometric factor is an important parameter of an instrument that specifies the shape and relative orientation of the source emitting radiation [33].

To convert the counts as a function of energy, angle and particle species into physical quantities such as flux and intensity, the total geometrical factor of an instrument must be known. The intensity, I, of incident particle distribution is related to the detector counting rate, C, as

$$C = GI \qquad (2.9)$$

where G is the geometric factor

It is an important task of space scientists and nuclear physicists to

be able to compute the intensity of radiation given the coincidence counting rate and the parameters of the instrument in an unknown radiation environment. So the calculation of geometric factor is important application in the analysis of data for a wide variety of experiments involving particle detectors.

2.7.1   Geometric Factor of two circular elements

For an isotropic source the geometrical factor depends only on the geometry of the telescope, i.e.

$$G = \int_{\Omega} d\omega \int_{s} d\sigma.\hat{r} \qquad (2.10)$$

The directional response function of a telescope, $A(\omega)$, can be defined as as

$$A(\omega) = \int_{s} d\sigma.\hat{r} \qquad (2.11)$$

where, $A = \int_{s} d\sigma$, is the surface area of the detector. So the directional response function can be visulized as the overlapped area between the detectors when one is parallel projected onto the other from direction ω. It has been eveluated from the symmetry of axis that $A(\omega) = A(\theta, \phi) = A(\theta)$, with no ϕ dependence [9].

For a telescope defined by two circular detectors of radii R1 and R2 respectively separated by a distance L as shown in Fig.2.12, the geometrical factor has been evaluated as [9]:

$$G = \frac{1}{2}\pi^2 \left[R_1{}^2 + R_2{}^2 + L^2 - \left[(R_1{}^2 + R_2{}^2 + L^2)^2 - 4R_1{}^2 R_2{}^2 \right]^{1/2} \right] \qquad (2.12)$$

By expanding and taking only the first order term for the case $L > R_1, R_2$ gives

$$G \geq \frac{A_1 A_2}{R_1{}^2 + R_2{}^2 + L^2} \qquad (2.13)$$
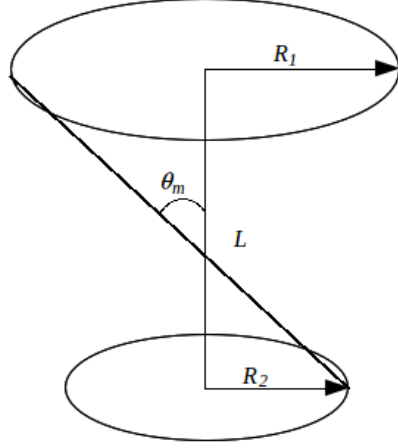
Figure 2.12: Two circular element particle telescope. [9]

2.7.2 Geometric Factor for three circular elements

For a telescope defined by three circular detectors of radii R_1, R_2 and R_3 separated by distances of L_{12}, L_{13} and L_{23} as shown in Fig. 2.13, the geometrical factor calculations become more involved. The Geometric factor, G_{123}, for the distinct three-element telescope can be evaluated as [9]

$$G_{123} = G_{13} - \pi^2 R_2^2 sin^2\theta + Z_{23}(\theta) + Z_{12}(\theta) - Z_{13}(\theta) \tag{2.14}$$

where

$$Z_{ij}(\alpha) = \int_0^\alpha 2\pi sin\theta A_{ij} d\theta \tag{2.15}$$

where, A_{ij} is the directional response function of any two of the three elements of the telescope.
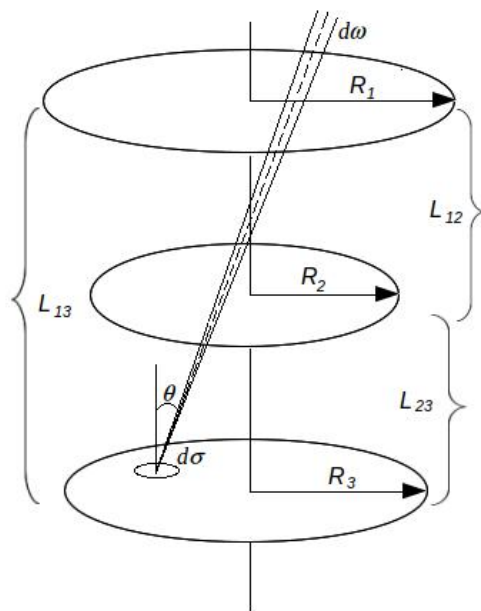
Figure 2.13: Three circular element particle telescope. [9]

Chapter 3

High Energy Head (HEH)

This chapter is dedicated to describing a detailed simulation model of the High Energy sensor Head (HEH). The simulations have been implemented in GEANT4 and detector response functions to the proposed electron and proton measurement values have been modeled to optimize the design. For these simulations the Electromagnetic Physics package of GEANT4 was used. This package includes basic energy loss and scattering interactions but does not include nuclear physics interactions which start to become important for protons above approximately 50 MeV. Thus if these aditional nuclear interactions were included there would be approximately a 10% decrease in channel efficiency for protons around 100 MeV. The inclusion of these aditional corrections is the subject of future work.

3.1   HEPT Design

The HEPT was designed to be one of the instruments to be mounted on ORBITALS which was aimed to measure electron and ion populations in the magnetosphere as well as dynamic electric and magnetic fields, waves and cold plasma to better understand space weather in the near-Earth environment. HEPT was designed to measure the angularly resolved high energy protons (3 - 120 MeV) and potentially energetic light ions and electrons.

The geometry, detector assembly and sweeping magnet design of HEPT was based on the PROTEL detector on the CRRES mission. The design was carried out using extensive high energy particle physics simulations using the GEANT4 Monte Carlo simulation code. Starting from the PROTEL design more detectors were incorporated to obtain higher energy resolutions and a higher geometric factor was used to give higher sensitivity to lower count rates. HEPT included two telescopes providing 2D coverage of energetic protons from 3 MeV to 120 MeV once per satellite spin. The measurements of very-high-energy inner belt and solar proton events were made possible by using a stacked silicon detector assembly and appropriate logic circuitry. The final baseline design comprised a High- Energy Head (HEH) sensor with a FOV of 36° and a Low-Energy Head (LEH) sensor with a FOV of 18°. It was required for the HEPT to be mounted in such a way that the FOV is unobstructed and the distance from the FGM (Flux Gate Magnetometer) is maximized to avoid interference from HEPT's shielding magnets. The HEPT might also examine the energetic electrons using the HEH sensor with energy coverage from 3 MeV to 26 MeV.

The LEH and HEH instrument designs are based on silicon detector stacks, which are located in detector cavities that are surrounded by metal shields. The shields prevent particles incident from outside the desired acceptance cone angle of the instrument from depositing energy in the detectors. The metal layers have been chosen to optimize this shielding process and limit the number of protons and electron that reach the detector stack from outside the defined Field Of View (FOV). These instrument heads are cylindrically symmetric except for the magnet sections in the LEH, which is intended to sweep out low energy electrons that enter the aperture of the HEPT.

The HEPT design is designed to be more sensitive and accurate than previous proton telescopes. The binning of deposited energy is defined for approximately 24 logarithmically-spaced energy channels in the range of 3 MeV to 120 MeV for the protons and 5 logarithmically-spaced energy channels in the range of 4 MeV to 26 MeV for the electrons. The optimum channel resolution, detector stack design and shielding have been be determined through simulation models in GEANT4 [31] before implementing a qualification test model to verify performance in a suitable environment and beam tests.

The count rate designed for is 20,000 proton counts per second in a quiescent proton flux environment at an altitude and orientation of maximum flux. The detector is designed to be able to measure 200,000 proton counts per second during high flux events without saturation. It is expected that our average count rate in the majority of the proton radiation belt will be in the neighbourhood of a few thousand proton counts per second. Similarly we expect solar maximum electron count rates for energies of 3 MeV and above of the order of a 2500 electron counts per second near L = 4. These count rates are based on the NASA AP-8 MAX and AE-8 MAX models and the CRRESELE Max model. The higher maximum count rates has been predicted up to the order of approximately 50,000 counts per second at L = 4 for electrons above 2 MeV during solar maximum [10], which is still well within the 200,000 counts per second range of the detector.

3.2   HEH

A high energy sensor head as implemented in GEANT4 simulation is shown in Fig. 3.1. A stack of silicon detectors is arranged in sequence to measure the particle energy based on the stopping power of that particle. The method of coincidence detection has been used to assure that the

energy deposition occured from a particle that enter from the designed FOV of the instrument. A front coincidence detector has been used for HEH. Only protons of energies greater than about 25 MeV can reach the detector stack through an entrance plate placed after the entrance cone of the instrument. Every proton that results in the counting of an event must pass through this detector to trigger the logic for the detector stack. This actively limits the acceptance angle to 36° giving a geometric factor of approximately 0.42 cm^2srad as will be discussed later in this chapter. The low energy particles deposit their energy in the first three detectors of the stack and the binning requirement for the particular bin is fulfilled according to the logic for that bin. If a proton of high enough energy is incident from the side or the back of the instrument it will pass through the shield and deposit some energy in the detectors but in most cases it is unlikely to deposit the correct amount of energy in the sequence of stack detectors so will not result in an increment of the count of any of the energy bin counters.

The detector cavity of high energy head is not as heavily shielded as that of the low energy head but the angular coincidence requirement reduces the effects of spurious events greatly. The cutoff energy, 72 MeV, for side incident protons is achieved with detector shielding of 1.5cm thick aluminum housing enclosing 0.25 cm thick tungsten. Electrons are cut off below 8 MeV by the side shielding. A 1 cm copper plate is added to the back and the back silicon detector used together to eliminate back penetrating high-energy particles. A signal on the back silicon detector will reject any signals being processed. The copper plate could be replaced by a lower activation material of equivalent mass and stopping power, such as tantalum, in an optimized design of the detector.

The high energy electrons in the range of 3 MeV to 26 MeV can be
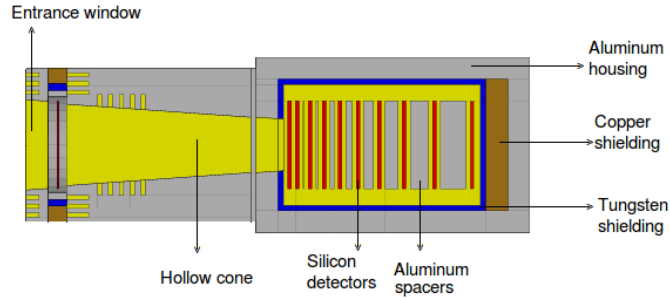
Figure 3.1: The HEH sensor as implemented in the GEANT4 simulation

measured simultaneously along with protons with the HEH. The addition of aluminum spacers reduces the logic for both proton and electron energy binning and reduces the voltage requirements, cost and complexity associated with very thick silicon detectors that would be required to achieve the maximum 120 MeV measurement which is the goal of HEPT.

3.2.1 Energy Deposition in Silicon Detectors

The scattering within the detector, especially for electrons, reduces the efficiency of detector from 100 % to measure an incident particle entering the FOV. In order to get significant information on both the energy deposition statistics in the detector heads as well as the counting efficiency for particles the HEPT detector heads have been simulated in GEANT4.

By using the stopping-power of silicon acquired from the NIST [34] the average energy deposition of protons and electrons in the silicon detectors has been calculated as a function of position.The generated charge distribution is calculated by assigning one charge pair generated for every 3.6 eV of energy that is deposited in the silicon. Using this relationship a proton with 1 MeV of kinetic energy that is completely stopped in a detector element will generate almost 280,000 charge pairs.

The high energy head measures the energies ranging from 27 MeV

44
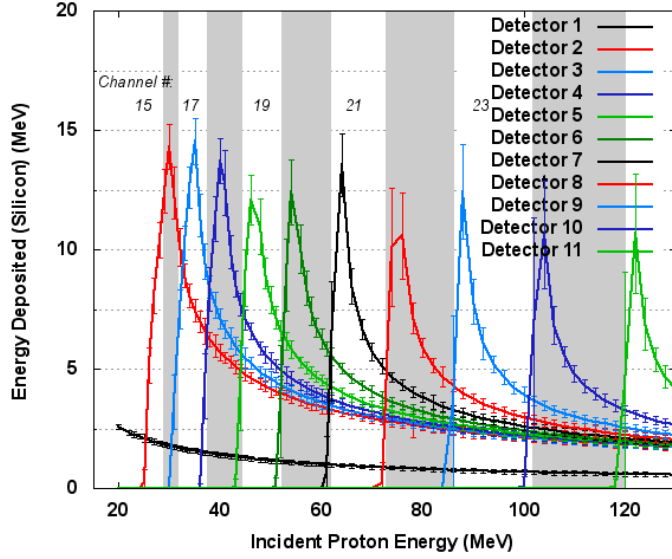
Figure 3.2: Proton energy deposition versus incident proton energy through the front aperture in the HEH by simulation.

to 120 MeV and comprises the last 9 of 24 logarithmically spaced energy bins. The average amount of energy deposited in each silicon detector is shown in Fig. 3.2. The line is the mean deposited value and the error bars represent the standard deviation of the calculated energy deposition. For protons the deposition of energy into the next silicon detector in the sequence coincides with a point from which the next channel is turned on. This is achieved by chosing appropriate thicknesses of the aluminum spacers along with detectors. Table3.1 lists the detector stack thicknesses and aluminum spacer thicknesses used to calculate the deposition curves in GEANT4.

Further improvement in the HEH detector stack may be possible with higher density tantalum spacers in place of the aluminum initially chosen as shown in Fig. 3.6. Tantalum reduces both the detector length and net angular scattering of the electrons in transit within the detectors. Fig. 3.6 shows a schematic of HEH with tantalum spacers used in simulations.

The detector responses to incident electrons modeled for the HEH

Detector No.	Thickness (μm)
1	500
2-11	1500
Spacer 1	200
Spacer 2	2562
Spacer 3	350
Spacer 4	960
Spacer 5	1700
Spacer 6	2758
Spacer 7	4155
Spacer 8	5870
Spacer 9	8380
Spacer 10	11600

Table 3.1: HEPT detector and Aluminum spacer thicknesses for HEH case

in GEANT4 is shown in Fig. 3.3. It is clear that scattering of electrons in the detector and spacer plates has reduced the actual number of electrons detected within a given energy bin and thus only a fraction of the electrons penetrate deeply into the detector and are counted.

Proton logic bin channels have been defined for each of the detector elements D2 to D10 and the key defining logic threshold values used in terms of deposited energy are given in Table 3.2 for the protons. In case of heavier particles, e.g. α-particles, the amount of energy deposited would be higher than by protons. The logic table would reject such particles so they will not be counted. The detector thicknesses and spacer thicknesses are chosen to give a sharp turn on of each additional detector channel given by the steep rise in deposited energy in each successive detector element. This leads to a robust design which reduces the background noise and additional baseline noise introduced by the much lower electron signals. This design is also robust against degradation in detector response due to radiation damage since it is based primarily by density penetration depth
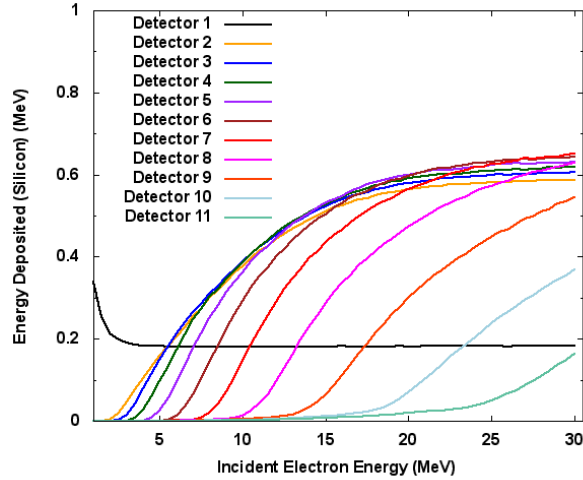
Figure 3.3: Simulation of electron energy deposition in the HEH of HEPT versus incident proton energy through the front aperture with the channel numbers indicated in the figure. The line is the mean value of the energy deposition.

which does not change with response degradation area. Table 3.3 gives the detector logic threshold values for electron energy channel bins.

Using these logic bin variables, energy channels have been defined for the protons and electrons. The detection efficiency per incident proton and electron within each such energy channel is shown in Figs. 3.5 and 3.4 respectively. Since the protons do not scatter significantly very well-defined channels are obtained as seen in Fig.3.5. Significant scattering occurs for the case of electrons and lower energy electrons < 8 MeV suffer large scattering losses from the 2.762 mm thick aluminum degrader plate at the entrance of the detector. This reduces the counting efficiency for these electrons to less than 10 %, but this reduced detection efficiency is beneficial in reducing the perturbation of a very large number of lower energy electrons on the lower energy proton channels and in extending the peak dynamic range for detection of anomalously high multi MeV electron fluxes during magnetic storms.

Channel	D1		D2		D3		D4		D5		D6	
MeV	Low	High	Low	High	Low	High	Low	High	Low	High	Low	High
26.9-31.7	0.4	100	7.5	20	0	6.36	0	0.4	0	0.4	0	0.4
31.7-37.5	0.4	100	6	20	6.35	20	0	6.15	0	0.4	0	0.4
37.5-44.2	0.4	100	4.6	20	5.4	20	6.15	20	0	5.21	0	0.4
44.2 - 52.2	0.4	100	3.7	20	4	20	4.6	20	5.21	20	0	4.82
52.2 - 61.6	0.4	100	3	20	3.1	20	3.4	20	4	20	4.82	20
61.6 - 72.9	0.4	100	2.5	20	2.6	20	2.7	20	3	20	3.4	20
72.9 - 86.0	0.4	100	1.9	20	2	20	2.1	20	2.3	20	2.6	20
86.0 - 101.6	0.4	100	1.7	20	1.7	20	1.8	20	1.9	20	2	20
101.6-120.0	0.4	100	1.4	20	1.5	20	1.5	20	1.5	20	1.6	20

Channel	D7		D8		D9		D10		D11	
MeV	Low	High	Low	High	Low	High	Low	High	Low	High
26.9-31.7	0	0.4	0	0.4	0	0.4	0	0.4	0	0.4
31.7-37.5	0	0.4	0	0.4	0	0.4	0	0.4	0	0.4
37.5-44.2	0	0.4	0	0.4	0	0.4	0	0.4	0	0.4
44.2 - 52.2	0	0.4	0	0.4	0	0.4	0	0.4	0	0.4
52.2 - 61.6	0	4.36	0	0.4	0	0.4	0	0.4	0	0.4
61.6 - 72.9	4.36	20	0	4.34	0	0.4	0	0.4	0	0.4
72.9 - 86.0	3	20	3.34	20	0	3.34	0	0.4	0	0.4
86.0 - 101.6	2.1	20	2.5	20	3.41	20	0	3.19	0	0.4
101.6-120.0	1.7	20	1.8	20	2.1	20	3.19	20	0	1.45

Table 3.2: Low and High logic bin threshold values used for protons for the HEH. [1]

49
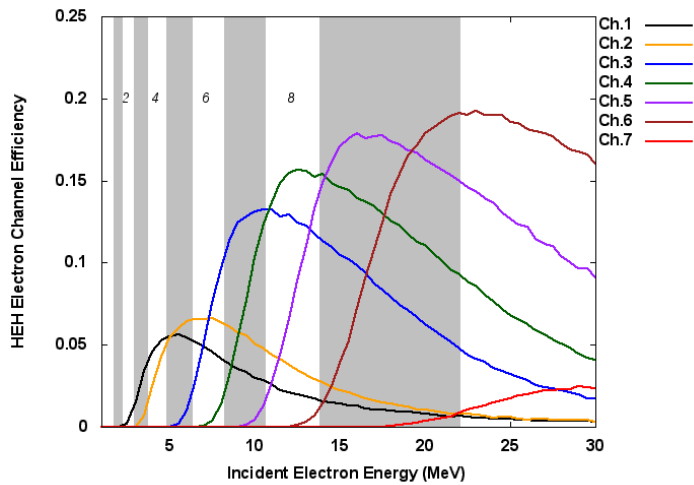
Figure 3.4: Detector Channel efficiencies for the High Energy Head: electron response. The plotted values are calculated using GEANT4 and represent the probability of an incident particle being detected within a given energy channel
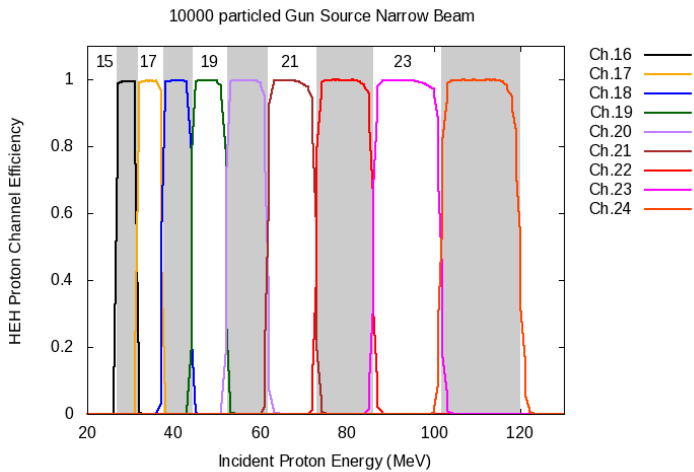
Figure 3.5: Detector Channel efficiencies for protons. The plotted values are calculated using GEANT4 and represent the probability of an incident particle being detected within a given energy channel

Channel	D1		D2		D3		D4		D5		D6	
MeV	Low	High	Low	High	Low	High	Low	High	Low	High	Low	High
Ch 1	0.12	1	0.4	4	0.4	4	0	0.4	0	0.4	0	0.4
Ch 2	0.12	1	0.4	0.8	0.4	2	0.4	4	0	0.4	0	0.4
Ch 3	0.12	1	0.4	0.8	0.4	0.8	0.4	2	0.4	4	0.4	4
Ch 4	0.12	1	0.4	0.8	0.4	0.8	0.4	1	0.4	1.2	0.4	2
Ch 5	0.12	1	0.4	0.8	0.4	0.8	0.4	1	0.4	1.2	0.4	1.2
Ch 6	0.12	1	0.4	0.8	0.4	0.8	0.4	1	0.4	1.2	0.4	1.2
Ch 7	0.12	1	0.4	0.8	0.4	0.8	0.4	1	0.4	1.2	0.4	1.2

Channel	D7		D8		D9		D10		D11	
MeV	Low	High	Low	High	Low	High	Low	High	Low	High
Ch 1	0	0.4	0	0.4	0	0.4	0	0.4	0	0.4
Ch 2	0	0.4	0	0.4	0	0.4	0	0.4	0	0.4
Ch 3	0	0.4	0	0.4	0	0.4	0	0.4	0	0.4
Ch 4	0.4	5	0	0.4	0	0.4	0	0.4	0	0.4
Ch 5	0.4	2	0.4	5	0	0.4	0	0.4	0	0.4
Ch 6	0.4	1.5	0.4	2	0.4	5	0	0.4	0	0.4
Ch 7	0.4	1.5	0.4	2	0.4	2	0.4	5	0	0.4

Table 3.3: Low and High logic bin threshold values used for electrons for the HEH [1]
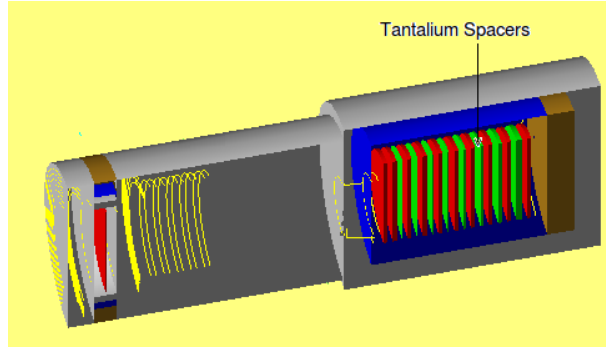
Figure 3.6: Tantalum HEH sensor as implemented in GEANT4 simulation

3.2.2 Counting Rate for Proton Detection

Fig. 3.7 from the AP8-MAX model [5] the maximum proton counting rates occur approximately at $L = 1.5$ R with count rates of the order of 2000 counts per second (cps) on the first detector element for proton energies above 26.9 MeV as shown in. The CRRESPRO-active proton flux model shown in Fig. 3.8 also predicts count rates of the order of 3000 counts per second on the first detector element for proton energies above 26.9 MeV. Digitization of a proton event is triggered by a valid count on the first detector element above 1.4 MeV together with a coincidence detector signal above 0.4 MeV on the coincidence detector to ensure that the particle has entered from the front aperture. Thus proton digitization will occur only at a rate of 2000 - 3000 cps under average solar maximum conditions. This allows an additional factor of 70 to 100 times dynamic range for extremely strong magnetic storms at a maximum count rate of 200,000 cps and an extra dynamic range of 170 to 250 times if we can achieve a maximum count rate of 500,000 cps. It is important to noted that very large increases in proton fluxes have been previously reported during magnetic storm events.
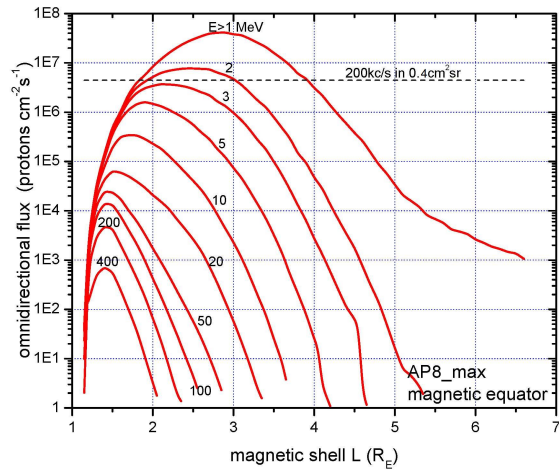
Figure 3.7: Predicted omnidirectional integral proton flux rates based on AP-8 Max.
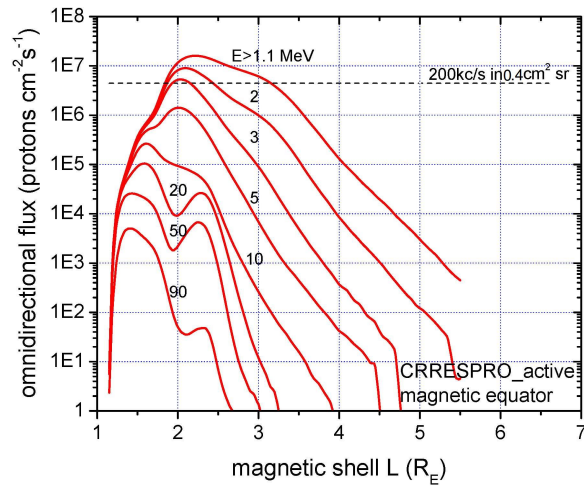
Figure 3.8: Predicted omnidirectional integral proton flux rates based on CRRES Max.
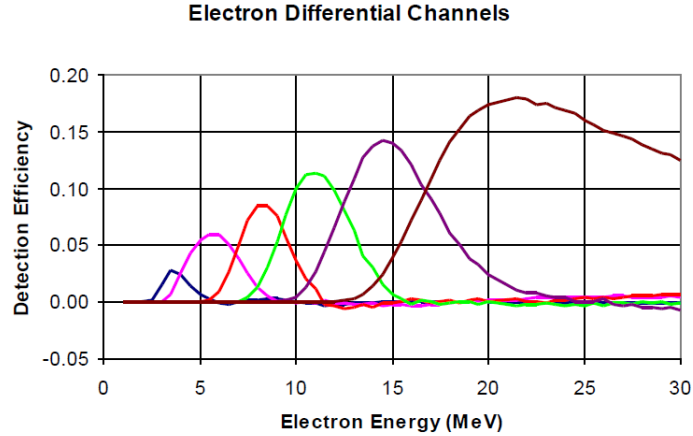
Figure 3.9: Differential electron channel

3.2.3 Counting Rate for Electron Detection

As described earlier, a very significant scattering occurs in the detector and spacer elements for the case of electrons leading both to reduced detection channel efficiency and to significant counting of higher energy electrons in lower energy channels since they can be scattered sideways in an earlier detector element. The resulting effect is that each detector element channel has a long tail as can be seen in Fig.3.4. Each channel acts somewhat like an integral channel detecting electrons above a threshold energy. Thus, in order to define more distinct energy bins these energy channels must be differenced again. Such a differencing algorithm has been developed and the resulting energy channels are shown Fig.3.9 and tabulated in Table 3.5 based on appropriate combinations of the above energy channels, given in Table 3.4.

It can be seen that the efficiency is low for the lower energy bins but this can compensate the much higher expected count rates for electrons in the lower energy bins and avoids saturation effects during the peak solar storm periods. Note that each real channel has a relatively sharp turn on threshold since electrons below a minimum energy cannot penetrate

	DC1	DC2	DC3	DC4	DC5	DC6
Ch 1	1	0	0	0.	0	0.
Ch 2	-0.9	1	0	0	0	0
Ch 3	0.2	-0.55	1	0	0	0
Ch 4	-0.1	0.2	-0.92	1	0	0
Ch 5	0	0.02	0.15	-0.85	1	0
Ch 6	0	0	0.08	0.15	-0.80	1
Ch 7	0	0.	0.	0.50	1.30	-1.5

Table 3.4: Detector channel weighting functions for electron energy bins

Differential Channel	Centroid (MeV)	Range FWHM (MeV)	Percentage width
DC1	3.7	3.0-4.5	40%
DC2	5.7	4.1-7.3	56%
DC3	8.4	6.9-9.7	33 %
DC4	11.1	9.0-13.2	38 %
DC5	15.15	12.6-17.7	34 %
DC6	>16.4	>16.4	

Table 3.5: Electron bin channels obtained by differencing of real detector channels
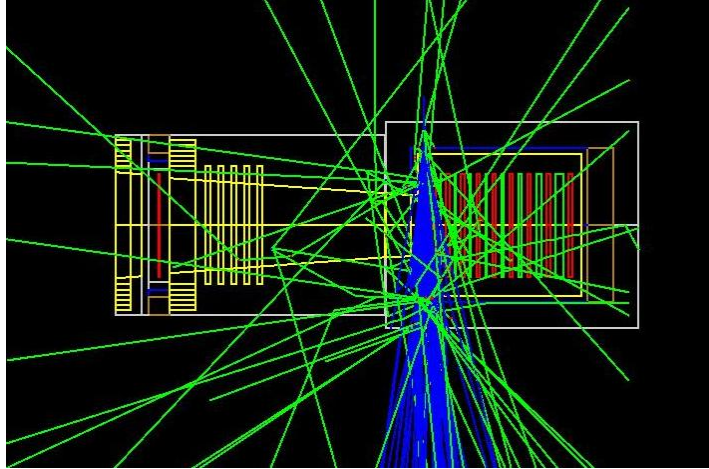
Figure 3.10: Figure shows 100 protons at energy 150 Mev penetrating through the side walls of the detector. The proton beam is placed at position above detector element D2.

through the integrated detector to arrive at the deeper detectors which gives the signatures for the existence of high energy electrons above the detection threshold for each detector channel.

Spurious events due to penetration of energetic particles from the side occur at a low count rate due to the thick wall shielding which will block protons below 72 MeV and electrons below 8 MeV. Furthermore these spurious events would also have to simultaneously trigger all the intermediate detector elements in order to be counted as a real event thus lowering the probability of such single spurious events being counted. Fig. 3.10 shows 100 protons penetrating from the side shielding at energy 150 MeV. The gun source was placed at position above the detector D2. Fig. 3.11 shows the energy deposition versus incident energy of protons from the side walls of the detector.

There are a number of models describing the maximum electron count rates expected during solar maximum and magnetic storm events. It is important to take into account magnetic storm events which are some of the prime events which we wish to characterize with the ORBITALS mis-
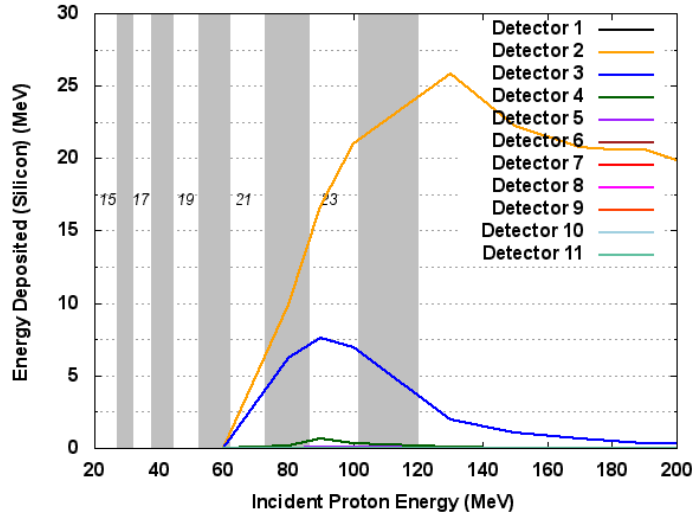
Figure 3.11: Plot of energy deposited in the detector elements versus incident energy of protons from the side shielding showing that maximum energy is deposited in D2, since the beam source was place above D2.

sion. For this purpose HEPT is designed to take into account the maximum electron and proton rates expected. Fig. 3.14 gives a plot of the solar maximum electron count rates expected from the AE-8 MAX model [6]. Also for comparison the electron fluxes predicted by the CRRESELE MAX model are given in Fig. 3.15. It can be seen that the peak count rates predicted for electrons above 2 MeV, which is the lowest electron energy which effectively can arrive at the first signal detector, D2, is on the order of 34,000 cps from the CRRESELE MAX model and the order of 26,000 cps from the AE-8 MAX model. However, the actual count rate at the first signal detector D2 is on the order of 20 times less than this since on the order of 95% of the low energy electrons below 5 MeV are scattered out of the acceptance aperture of the first signal detector (as can be seen from Fig. 3.9). Thus the expected count rates for the lowest energy electron channel (3.0-4.5 MeV) is of the order of 2,000 cps based on the CRRESELE MAX model or a factor of 100 times below the current maximum count rate of
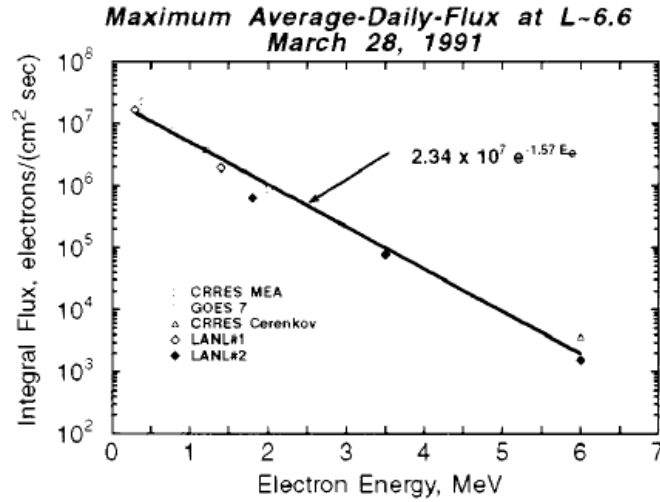
Figure 3.12: Plots of electron flux showing the daily average omnidirectional integral flux for the highest signal cases of CR-RES, GOES and LANL ©2000, IEEE [10].

200,000 cps. However, this large dynamic range is required to cover the sharp increases which can occur during strong magnetic storms.

The required extra dynamic range can be estimated from highest data ever observed from the CRRES and GOES missions. Peak flux data has been fit by Fennell et al. 2000 [10] as shown in Figs. 3.12 and 3.13. Fig. 3.12 gives an exponential fit to the data and Fig. 3.13 is a scaling with observation time to give the peak short time flux compared to AE8-MAX for L= 6.6. It is seen that the peak values are 53 times higher than the AE-8 Max model for electrons above 2 MeV at L =6.6. These can be used to estimate the maximum values which the ORBITALS mission might see under similar conditions. The daily averaged omnidirectional integral electron spectrum given by Fennell et al. [10]

$$F = 2.34 \times 10^7 \exp(-1.57 \times E_{MeV}) \ electrons/cm^2/s \qquad (3.1)$$

It was found from Fig. 3.13 that the peak flux for a short measurement interval was 1.6 times higher than the daily average during the peak

58
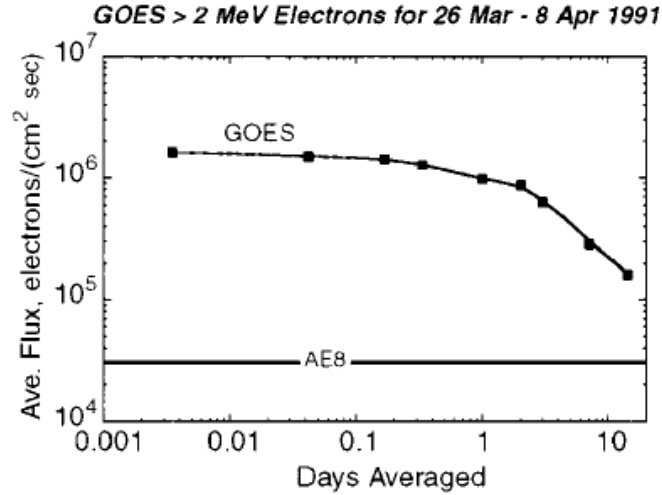
Figure 3.13: Plots of electron flux scaling with observation time during the peak flux period ©2000, IEEE [10].

storm period. Taking into account this factor of 1.6 and the geometric factor value of HEH detector 0.4 cm2 srad predicted integral flux of electrons at L = 6.6 into our detector is given as

$$F_{MeV} = 0.78 \times 10^6 \exp(-1.57 \times E_{MeV}) \; electrons/s \qquad (3.2)$$

The predicted count rate above 2 MeV would be approximately 34,000 cps entering our detector. From AE8- MAX the peak flux at L = 4 is approximately 15 times higher than at L = 6.6 leading to an estimated peak flux of 510,000 cps entering the detector at L = 4. Due to scattering of the electrons in the entrance degrader plate, only about 5% of these electrons will trigger the first signal detector and thus the resulting count rate of approximately 26,000 cps will be well within the 200,000 cps maximum count rate of the detector. This is about 20 times the predicted solar maximum flux from the CRRESELE model.
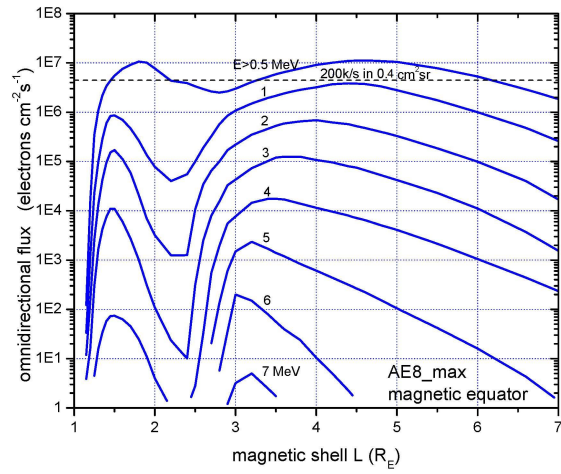
Figure 3.14: Predicted omnidirectional integral electron flux rates based on AE-8 Max.
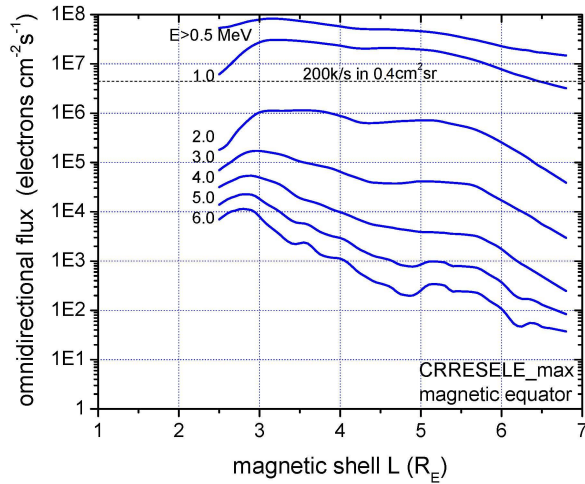
Figure 3.15: Predicted omnidirectional integral electron flux rates based on CRRESELE Max.
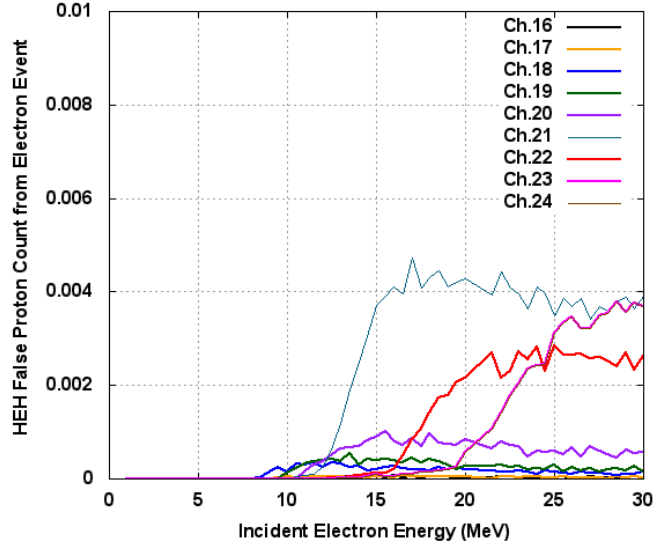
Figure 3.16: GEANT4 simulation of the rate of false counts in proton detector channels per electron from incident electrons

3.2.4 Electron and Proton Interference

The effect of even a high rate of fluence of electrons on the proton channels is small. Since the deposited energy per electron passing through a detector element is on the order of 5 to 10 times less than a proton passing through the detector element, the trigger threshold for proton events is set much higher at 1.4 MeV deposited for protons than for electron events which is at 0.4 MeV. Electrons can scatter and can cause false trigger signals and false detector counts by scattering through the detector elements at skew angles. The rate of false counts in the proton channels per incident electron has been estimated, for HEH with aluminum spacers, using GEANT4 and is plotted in Fig.3.16 as a function of electron energy. This count rate is less than and of the order of 0.1% for electrons in the range of 8 MeV to 12MeV and of the order of 0.4% for electrons above 12 MeV energy. From equation (3.2) corrected by a factor of 15 from L=6.6 to L=4 which is the worst expected case for the incidence rate of electrons above 8 MeV the expected electron rate is less than the order of 100 per second.

61

Thus if the order of 0.1 percent of these electrons give false proton counts this would lead to the order of 0.1 false counts per second which is close to the expected noise floor of 0.1 cps for proton detection. Note, again these electron flux rates are 20 times the normal peak values expected from the CRRESELE MAX model and would represent an extreme case likely only to occur once or twice during the ORBITALS mission.

3.3   Geometric Factor calculations for HEH

In space the particles can enter the detector at any angle within the acceptance cone angle of the detector. Some particles coming at an angle to the axis will stop in shorter axial distance and could appears as a lower energy particles in some cases to the detector. In order to estimate the geometric factor for HEH three approaches have been used as outlined in the following sections.

3.3.1   Geometric Factor for Three Circular Elements

For the HEH case $R_2 = 1.1766cm$ defines the limitting angle θ_m. Any particle entring at this maximum angle cannot hit the last few detector elements. In this case a three circular element geometry (shown in Fig. 2.13) is used to calculate the geometric factor. Since higher energy particles penetrate deep through detectors so far 70 MeV proton which can penetrate up to D7 which is at distance L_{13} =14.83 cm from D1. By using equation(2.14) the value of geometric factor for for 30 MeV and 70 MeV is G = 0.42 $cm^{-2}srad^{-1}$. In this case $R_1 = 2.062cm$, $R_2 = 1.1766cm$ and $R_3 = 2cm$ with distances $L_{12} = 11.5$ cm between D1 and D2, $L_{13} = 14.83$ cm between D1 and D7 and $L_{23} = 3.33$ cm between D2 and D7. Similarly for 105 MeV proton which penetrates upto D10 with L_{13}=18.3223 cm and L_{23}= 6.8 cm the value of G= 0.33 $cm^{-2}srad^{-1}$. Thus the geometric factor

is a function of proton energy for the present detector design.

3.3.2   1D Beam source for HEH

For the first calculation a 1D circular beam source was taken in the GEANT4 simulation. The radius of the source is 3 cm so that it is larger than the opening of the entrance cone and it is placed 0.5 cm away from the detector entrance. For the simulations a 1D beam with 100,000 particles each of energy 30 MeV, 70 MeV and 105 MeV and with increasing angles of incidence of from $0 - 20^0$ in 2.5^0 increment were used. An example layout plot from GEANT4 simulation is shown in Fig.3.17.

The particles are binned into 9 energy channels by applying the standard energy bin logic as given in Table 3.2. When the particles enter at some axial angle θ their integrated axial range through solid is lowered by a factor of $cos\theta$. Also they can enter the detector by scattering process and through a thinner section of the front shielding window which can be seen in Figs.3.17(a) and 3.17(b) which also lowers the energy of incident particles. Thus some of the particles will not deposit energy in the correct detector channel and may sometimes be counted in the wrong channel. This will causes false count of particles. It is very important to estimate false counts in order to characterize the detector response properly. The incoming particles hit the detector and can go to the correct channel or wrong channel. According to the acceptance logic three types of histograms have been plotted as:

(i) Sum of counts in all channels versus angle

(ii) Counts in the correct channel versus angle

(iii) Sum of counts in the wrong channels versus angle for each energy.

Since the 1D beam makes an angle θ with the axis, the effective source area of the beam $A_{acceptance}$, which is the overlapping area of the
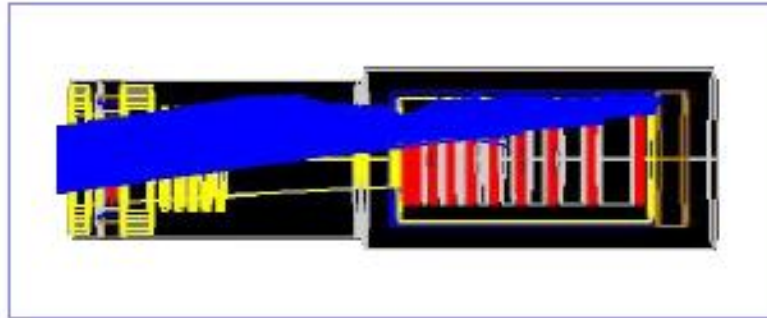
(a) 1D beam source at an axial angle of 10^0 and fixed value of ϕ for the HEH
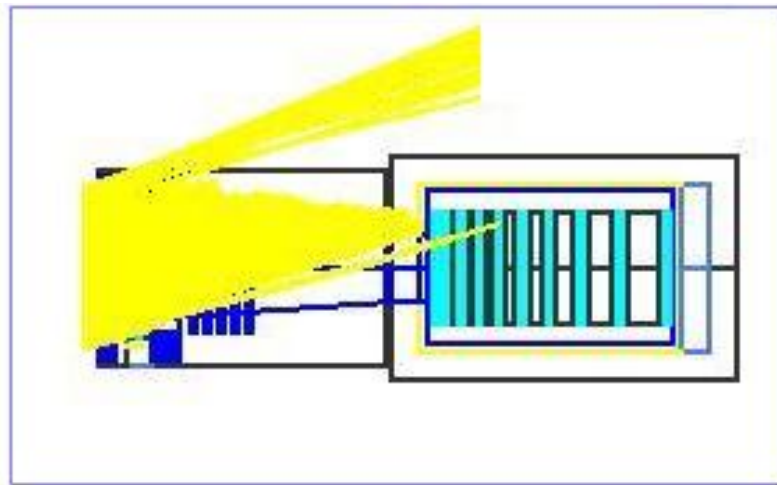
(b) 1D beam source at an axial angle of 20^0 and fixed value of ϕ for the HEH

Figure 3.17: 1D beam source as implemented in GEANT4 simulation

source and the entrance window, is reduced by a factor of $cos\theta$. The effective acceptance area for each angle has been calculated as

$$A_{acceptance}(\theta) = \frac{n}{F} \qquad (3.3)$$

where n is the number of counts that hit the detector and F is the flux per unit area of the source, calculated as given below

$$F = \frac{N}{A} \qquad (3.4)$$

where A is the area of source and N is total number of events emitted by the source.

The ith value of geometric factor for isotropic flux at a particular energy can be calculated as

$$g_i = A_{acceptance}(\theta_i)\Omega_{\theta_i} \qquad (3.5)$$

where $A_{acceptance}(\theta_i)$ and Ω_{θ_i} correspond to the ith value of acceptance area and solid angle. In order to calculate the total geometric factor from 0^0 to 12.5^0, it was assumed that $A_{acceptance}(\theta)$ remains constant within an angular range of $(\theta - \delta\theta)$ and $(\theta + \delta\theta)$, where $\delta\theta$ is taken as 1.25^0. For example, the geometric factor from 0° - 2.5^o has been calculated as

$$g_{(0-2.5)} = \int_0^{2\pi} d\phi \left(A_{acceptance(0-1.25)} \int_0^{1.25} sin\theta d\theta + A_{acceptance(1.25-2.5)} \int_{1.25}^{2.5} sin\theta d\theta \right) \qquad (3.6)$$

So the total geometric factor, G, has been calculated by taking the sum of the partial geometric factor, g, for a particular value of angle θ, as given below

$$G = \sum_j g_j \qquad (3.7)$$

Fig. 3.18 shows a decreasing acceptance area of the disk source with increasing incident angle. This decrease in overlapping area will decrease
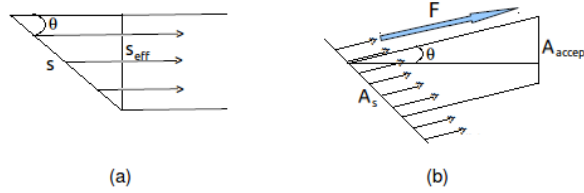
Figure 3.18: Diagram of tilted source layout used in the simulation showing how (a) effective source is smaller by a factor of $cos\theta$, (b) Acceptance area, A_{accep}, of the source.

Energy (MeV)	Angle (degree)								
	0^0	2.5^0	5^0	7.5^0	10^0	12.5^0	15^0	17.5^0	20^0
30 MeV	4.29	4.29	3.99	3.1	1.96	.83	.13	.01	0
70 MeV	4.86	4.9	4.69	3.8	2.75	1.75	.8	.17	0
105 MeV	6.02	6.02	5.96	5.14	3.74	1.95	0.87	.46	0

Table 3.6: Acceptance area for total number of counts for each individual subangle

the number of particles hitting the detector i.e. a decrease in number of counts. It is important to note that instead of using a tilted source, a source with 1D beam tilted at certian angle has been used i.e. the beam is making an angle with the source through which it is emitting. This geometry gives approximately the same flux at small values of θ. Here it was assumed that $A_{acceptance}(\theta)$ remains constant within an angular range of $(\theta - \delta\theta)$ and $(\theta + \delta\theta)$, where $\delta\theta$ is taken as 1.25^0. The individual geometrical factor, calculated by using Eqn.(3.5), for all the counts, the correct counts and the wrong counts are listed in Table 3.7, 3.8 and 3.9 at each angle respectively. Figs.3.19, 3.20 and 3.21 show the $A_{acceptance}$ for corresponding angle at 30 MeV, 70 MeV and 105 MeV for all, correct and wrong channel counts. The acceptance areas corresponding to individual subangle for 30 MeV, 70 MeV and 105 MeV are listed in Table 3.6.

The geometrical factor calculated by 1D beam source for increasing θ from 0 to 20^0 for total, correct and wrong counts is listed in Table 3.10.
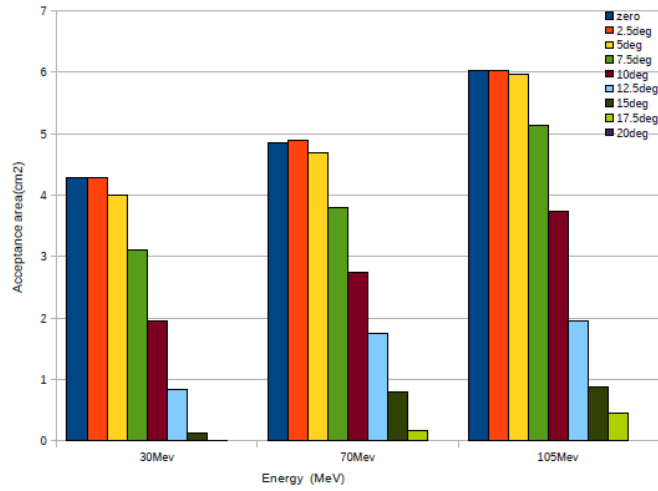
Figure 3.19: Effective $A_{acceptance}$ from the GEANT4 simulations for the counts detected in all channels vs angles for the HEH case.
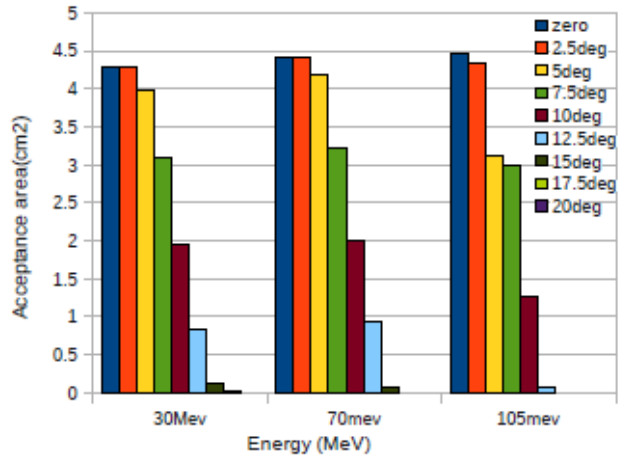
Figure 3.20: Effective $A_{acceptance}$ from the GEANT4 simulations for the counts detected in the correct channels vs angles for the HEH case.
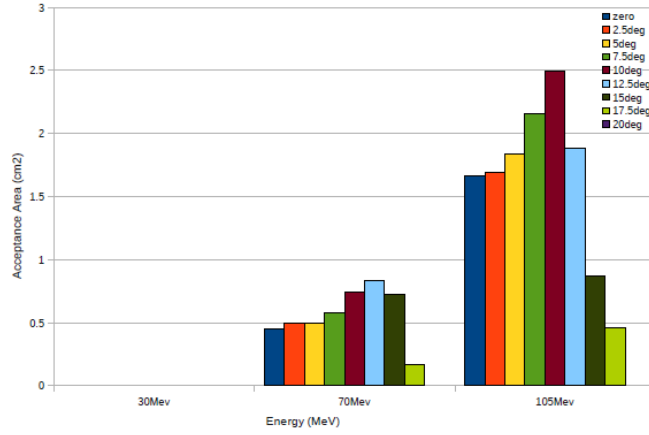
Figure 3.21: Effective $A_{acceptance}$ from the GEANT4 simulations for the counts detected in the wrong channels vs angles for the HEH case.

Angle	30 MeV	70 MeV	105 MeV
0^0- 2.5^0	0.0064	0.006	0.006
2.5^0- 5^0	0.05	0.057	0.072
5^0- 7.5^0	0.094	0.113	0 .142
7.5^0- 10^0	0.113	0.14	0.182
10^0 - 12.5^0	0.094	0.132	0.176
12.5^0- 15^0	0.05	0.1	0.115
15^0- 17.5^0	0.006	0.057	0.062
17.5^0- 20^0	0	0.013	0.038
20^0-22.5^0	0	0	0

Table 3.7: Individual geometric factor given by eqnuation (3.5) for each sub angular range for the counts detected in all channels for the HEH case

Angle	30 MeV	70 MeV	105 MeV
0^0- 2.5^0	0.0064	0.00554	0.0056
2.5^0- 5^0	0.05	0.0525	0.05166
5^0- 7.5^0	0.094	0.0999	0 .07445
7.5^0- 10^0	0.113	0.11526	0.10667
10^0- 12.5^0	0.094	0.132	0.05966
12.5^0- 15^0	0.05	0.0543	0.00413
15^0- 17.5^0	0.006	0.00588	0
17.5^0- 20^0	0	0	0
20^0- 22.5^0	0	0	0

Table 3.8: Individual geometric factor for each sub angular range for the counts detected in correct channels for the HEH case

Angle	30 MeV	70 MeV	105 MeV
0^0- 2.5^0	0	0.000565	0.0021
2.5^0- 5^0	0	0.00597	0.02
5^0- 7.5^0	0	0.0119	0 .0439
7.5^0- 10^0	0	0.0207	0.077
10^0- 12.5^0	0	0.0353	0.1188
12.5^0- 15^0	0	0.0543	0.1109
15^0- 17.5^0	0	0.0511	0.620
17.5^0- 20^0	0	0.013	0.0380
20^0- 22.5^0	0	0	0

Table 3.9: Individual geometric factor for each sub angular range for the counts detected in wrong channels for the HEH case

Energy	G_{total}	$G_{correct}$	G_{wrong}
30 MeV	0.41±0.0016	0.41±0.0	0.00±0.0
70 MeV	0.62±0.0022	0.43±0.002	0.187±0.0015
105 MeV	0.79±0.0024	0.302±0.0012	0.473±0.0022

Table 3.10: Total Geometric Factor for the all, correct and wrong channel counts.

It is the sum of geometrical factors at each angle for a particular energy.

3.3.3 Geometric factor by taking an isotropic source with limited angle for HEH

By using another approach for the second calculation of geometric factor an isotropic source was used to produce isotropic flux. For such an isotropic source most of the particles from the source will miss the detector and will make the calculation inefficient. For a circular and cylindrical symmetry the source angular range can be limitted between 0 and θ_m to get more efficient results. The maximum geometric acceptance angle is given by

$$\theta_m = tan^{-1}(R1 + R2)/L \qquad (3.8)$$

This is shown on Fig.2.13. Ideally for an entrance cone defined by two disks no count will be detected when $\theta > \theta_m$ but due to scattering form the cone and penetration of energetic particles from the front window shielding some particles can still hit the detector and can contribute to false channels.

A circular disk source of radius 3 cm is defined to emit particles in a solid angle 0.3789 srad by taking ϕ from 0-2π and θ from 0-20°, where 20° is the maximum value of θ. From the approach used in section(3.3.2) it can be seen that no count can be detected beyond this angle. Sources emitting 100,000 particles, with energies 30 MeV, 70 MeV and 105 MeV each, were used in the calculations. The particles will deposit energy while passing through the array of detectors. After satisfying the logic table they

Energy	C_{total}	$C_{correct}$	C_{wrong}
30 MeV	3829	3829	0
70 MeV	5827	4022	1805
105 MeV	7472	3032	4440

Table 3.11: Counts in all, correct and wrong channels for isotropic source with 20^0 halfwidth angle for HEH .

Energy	G_{total}	$G_{correct}$	G_{wrong}
30 MeV	0.4097±0.0066	0.4097±0.007	0 ±0
70 MeV	0.624±0.0082	0.431±0.007	0.193±0.0045
105 MeV	0.80±0.0093	0.325±0.006	0.475±0.0071

Table 3.12: Total Geometric Factor for the all, correct and wrong channels for isotropic source with 20° halfwidth angle for HEH.

can be considered as a count. From equation(2.9) the flux per unit area per sterradian for the source solid angle 0.3789 is given by:

$$I = 9343.99 cm^2 srad^{-1} \tag{3.9}$$

where I is the flux per unit area per sterradian. Table 3.11 and 3.12 lists the number of counts and geometric factor for the all, the correct and the wrong channels for isotropic source with 20° halfwidth angle for HEH.

3.3.4 Discussion

The two approaches in sections (3.3.2) and (3.3.3) shows that the total geometrical factor is large when the energy of particles is high. However the value of G for correct counts and wrong counts is comparable at high energies. At these higher energies, processes such as scattering and penetration through the edges of the apertures becomes important in creating false counts. When a high energy particle enters the front window of the detector it may be scattered by the walls of the cone and lose some of its energy. This will be detected as a lower energy particle and will contribute

in the wrong energy bin. High energy particles can also penetrate through the edges of front shielding and again can be detected in the wrong channel by losing some of their energy in penetrating through the shielding.

Particles entering at some angle θ to the axis can also appear at lower energy by a factor of approximately $cos\theta$, which will also contribute to count in the wrong channel. This is seen to be the case for larger angles of 10^0 where more false counts are detected at 105 MeV than correct counts. Thus for the higher energy channels a maximum cone angle of 20^0 total width only may be useful. Larger cone angles primarily leads to larger false counts.

A proton of 30 MeV deposits most of it energy in D2 detector similarly 70 MeV proton deposits most of its energy in D7 and 105 MeV proton in D10. The geometric factor calculated by [9] for D2 and D7 is G= 0.42 $cm^{-2}srad^{-1}$ and for D10, G= 0.33 $cm^{-2}srad^{-1}$. If we compare the results of the two simulation approaches used in sections (3.3.2) and (3.3.3) with each other we can see that the values of G for correct channels are in good agreement at, 30 MeV with an error 0.07%, 70 MeV with an error of 0.2% and at 105 MeV with error about 7.6% which indicates that the basic summation technique over subangles is correct. In this case the energies selected are not at the center but well inside the bin range. The basic geometric calculations given in sections (3.3.1) show that for 30 MeV and 70 MeV the values of G are in good agreement (**2.4% error**) with those calculated by simulations in sections (3.3.2) and (3.3.3). For 105 MeV the value of G in the correct channels have a discrepancy of about 9% from the simple geometric calculation. This large values of G calculated by simulations at high energy were expected since scattered particles deposit their energy energy in any stack detector. At lower energies the particles cannot penetrate through the edges of the entrance window but higher energy

72

particles can penetrate through and can scatter and deposit energy even if they do not enter the entrance cone of the instrument which may contribute in increasing the value of G. Furthermore the higher energy protons entering at larger angles or scattered from the sides deposited energies in the lower channels and may be counted as lower energy particles leading to false counts. But it appears that scattering of high energy particles from around the entrance cone edge can also enhance the count rate in the high energy channels leading to a large effective geometric factor than expected. For the higher energy channels the GEANT4 calculations for correctly counted particles show that approximately half the particles are scattered into incorrect channels.

3.4 Conclusion

The observed value of geometrical factor is in good agreement with the theoretical values. At high energies it has a **48%** error for counts in HEH as currently configured. At higher energies an increase in the value of G could be due to the spurious events scattered by the inner walls or through other detectors in the stack. The incorrect counts can be reduced by decreasing the acceptance angle of the entrance cone.The angular and energy dependent data describes the detector response function in detail and in the future could be used to correct raw measured data using iterative deconvolution routines. However it appears that the large acceptance angle of the current HEH design leads to many wrong counts at larger entrance angles and thus these larger angles are not contributing effectively to the signal. In this case future improvements probably should choose a somewhat smaller entrance cone angle for the HEH.

Chapter 4

Low Energy Head of HEPT

This chapter describes a detailed simulation model of the Low Energy sensor Head (LEH). The simulations have been implemented in GEANT4 and detector response functions to low energy proton have been modeled. For simulating LEH also, the Electromagnetic Physics package of GEANT4 was used.

4.1   LEH Design

The LE sensor Head comprises 5 silicon stack detectors along with an anti coincidence ring. An aluminum foil filter of 80 μm is placed before the sweep magnet assembly as shown in Fig.4.1 to remove electrons below a cut-off energy. Since the LEH provides low energy proton coverage the logarithmic spacing is achieved by using the silicon detectors of thickness listed in Table 4.1. The thickness of aluminum foil at the entrance is such that it will allow protons with energies greater than 2 MeV to pass though, eliminating a large number of low energy protons and electrons from the background signal in the proton detectors. The sweeping magnet is also used to divert the electrons away from the detectors. Such electrons can also produce an enhanced background noise count. A field strength of 5 kG is employed which eliminates electrons < 3 MeV in the LEH.

The LEH is designed with heavy shielding that is intended to stop

the largest possible number of off-angle protons from reaching the detector cavity and is especially thick for protons that are close to the correct trajectory for correctly triggering the detectors as can be seen in Fig. 4.1. The designed geometric factor of the LEH is 0.03 cm^2 srad.

The instrument is well-shielded for the protons incident from the sides. For protons incident at the detector stack assembly, directly normal to the nominal beam axis, the shielding is provided by 0.5 cm of aluminum, 1 cm of brass or copper and 0.25 cm of tungsten. Protons of energies up to approximately 110 MeV can be stopped by this amount of shielding. Only a few hundred protons above 110 MeV are expected in the LEH every second because based on the expected flux rate. Of these very few will meet the energy and coincidence conditions to correctly be registered as a proton of particular energy due to the coincidence requirement and energy binning. The stopping power of 110 MeV protons does not include the energy loss that protons will experience when passing through the skin of the satellite or the other instruments. Thus the number of such spurious protons will be further decreased. The shielding will also stop electrons below an energy of 8 MeV. The number of higher energy electrons entring the detector through the side shielding is estimated to be approximately 100 counts per second or even less than that [10]. Again, only a small fraction of these will satisfy the require energy deposition conditions to be counted as a proton. For proton measurements the shielding thickness of the tungsten may be increased by another 2 mm in regions of high electron background if required. Thus very clean measurements without electron interference may be obtained.
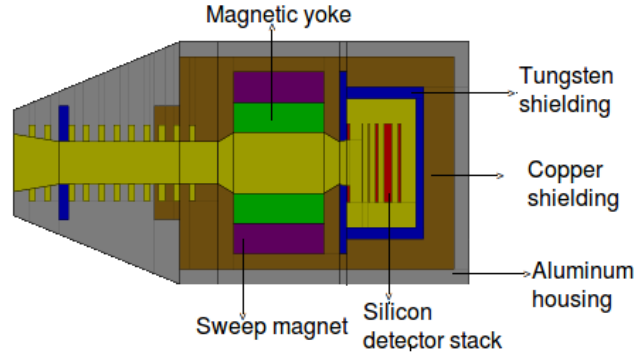
Figure 4.1: The LEH sensor head as implemented in the GEANT4 simulation including detector positions and the sweeping magnet assembly.

4.1.1 Energy Deposition and Logic Bin

For the low energy head, The protons of energy ranging from 3 MeV to 26 MeV are measured by the low energy head in the first 15 of 24 energy bins as shown in the shaded bands in Fig. 4.2. Protons while passing through the silicon detectors deposit a fraction or all of their energy and each energy bin was determined based on the energy deposition measured in each detector and a set of logic thresholds giving a unique range of signals for each energy bin. Table 4.2 gives the low and high values for the allowed energy range deposited by protons in the LEH to satisfy the logic requirements for each energy bin. This Table was developed by Craig Unick (Laser Plasma Group, University of Alberta). These energy deposition tables are based on relations for protons passing through silicon and aluminum. The energy depositions for a particle stopping in a slab is linear and approximately equal to the incident energy. If the particle has sufficient energy to pass through the slab the deposited energy reaches a maximum value and then drops off sharply as the particle energy is increased. If a proton with a certain energy deposits some energy within the allowed low to high range of a particular channel it will be counted in that channel by incrementing in the number of events counted by one. Fig. 4.3 gives the channel response

Detector No.	Thickness (μm)
A/C Ring	1000
1	100
2	300
3	1000
4	2500
5	1000

Table 4.1: HEPT Silicon detector thicknesses for LEH case

function for incident protons in 15 well defined channels. It can be seen that the model calculations predict high detection efficiency and channel fidelity as compared to desired channel energy bins.

Channel No.	Energy(MeV) Range	D1 (MeV)		D2 (MeV)		D3 (MeV)		D4 (MeV)		D5 (MeV)	
		Low	High	Low	High	Low	High	Low	High	Low	High
Ch 1	3-3.47	0.3	1.5	-1.0	0.4	-1.0	0.4	-1.0	0.4	-1.0	0.4
Ch 2	3.47-4.02	1.5	2.3	-1.0	0.4	-1.0	0.4	-1.0	0.4	-1.0	0.4
Ch 3	4.02-4.65	2.3	3.5	-1.0	0.4	-1.0	0.4	-1.0	0.4	-1.0	0.4 4
Ch 4	4.65-5.38	0.4	100	0.4	2.2	-1.0	0.4	-1.0	0.4	-1.0	0.4
Ch 5	5.38-6.23	0.4	100	2.2	3.61	-1.0	0.4	-1.0	0.4	-1.0	0.4
Ch 6	6.23-7.21	0.4	100	3.61	4.97	-1.0	0.4	-1.0	0.4	-1.0	0.4
Ch 7	7.21-8.34	0.4	100	4.97	6.5	-1.0	0.4	-1.0	0.4	-1.0	0.4
Ch 8	8.34-9.66	0.4	100	0.4	100	.40	4.03	-1.0	0.4	-1.0	0.4
Ch 9	9.66-11.17	0.4	100	0.4	100	4.03	6.56	-1.0	0.4	-1.0	0.4
Ch 10	11.17-12.93	0.4	100	0.4	100	6.56	9.03	-1.0	0.4	-1.0	0.4
Ch 11	12.93-14.97	0.4	100	0.4	100	9.03	12	-1.0	0.4	-1.0	0.4
Ch 12	14.97-17.32	0.4	100	0.4	100	.4	100	0.4	7.43	-1.0	0.4
Ch 13	17.32-20.05	0.4	100	0.4	100	.4	100	7.43	11.99	-1.0	0.4
Ch 14	20.05-23.2	0.4	100	0.4	100	.4	100	11.99	16.35	-1.0	0.4
Ch 15	23.2-26.85	0.4	100	0.4	100	.4	100	16.35	21	-1.0	0.4

Table 4.2: Low and High logic bin threshold values used for protons for the LEH case

4.2   Geometric factor calculations for LEH

In order to calculate the geometric factor for LEH three approaches have been used. In the first approache the value of G has been evaluated from the mathematical approximation proposed by [9]. The two other approaches are based on the results obtained from the simulations. For the simulations two different methods have been implementd by using GEANT4 toolkit [?]. The three approaches are outlined in the following sections.

4.2.1   Geometric Factor for Two Circular Elements

For LEH case the silicon detector stack has short length so two circular element geometry can be used to calculate the geometric factor. For a telescope defined by two circular detectors of radii R_1 and R_2 respectively separated by a distance L, the geometrical factor has been evaluated from equation 2.12. So the value of G, for LEH, for $R_1 = 0.95cm$ and $R_2 = 0.7cm$ seperated by a distance $L = 11.2cm$ is calculated as 0.0309 $cm^2 srad$. Here R_1 and R_2 are the radii of front opening window and the inner opening window and L is the distance from R_1 to R_2.

4.2.2   1D Beam Source

For the first calculation a 1D circular beam source was taken in the GEANT4 simulations. A circular source of radius 1.5 cm was placed at a distance of 0.5 cm from the front entrance window of the detector. Since the aperture of the front opening window is 0.95cm, the source area is larger than the detector entrance aperture area which was flooded by the incoming particles. For the simulations a 1D beam with N=100,000 particles each of energy 5 MeV, 12 MeV and 21.5 MeV each was used. The angle of incidence of the 1D beam, θ, was increased from 0^0 to 12.5^0 with an
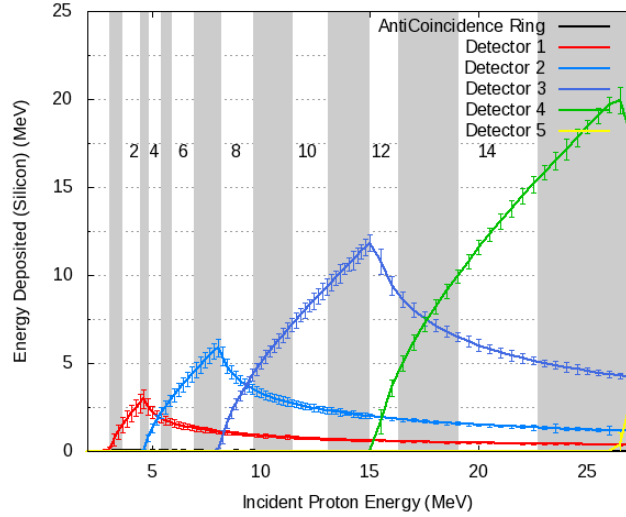
Figure 4.2: Simulation of proton energy deposition in the LEH of HEPT versus incident proton energy through the front aperture with the channel numbers indicated in the figure.

increment 2.5^0. Fig. 4.4 shows an example layout of 1D beam source emitting particles at 7.5^0.

The particles are binned into 15 energy channels by applying the standard energy bin logic as given in Table 4.2. When the particles enter the detector parallel to the axis they are well-binned as shown in Fig. 4.3. It can be seen that incident energies are well-binned in different channels for particles entering at 0^0 along the axis. The assigned energy of the particles is lowered by a factor of approximately $cos\theta$ when they enter at some angle θ to the axis since their penetration depth is reduced by a factor of $cos\theta$. There is also scattering of particles within the walls of the detectors. Thus some of the particles may deposit energy in the wrong channel, so it is important to estimate false counts as well to characterize the detector response properly. The incoming particles hit the detector and can go to the correct channel or wrong channel. According to the acceptance logic three types of histograms have been plotted as:

(i) Sum of counts in all channels versus angle

Energy (MeV)	Angle (degree)					
	0^0	2.5^0	5^0	7.5^0	10^0	12.5^0
5 MeV	1.23	0.91	0.45	0.099	0.0026	0.0004
12 MeV	1.41	0.99	0.489	0.094	0.0017	0.0006
22.5 MeV	1.47	1.03	0.493	0.091	0.0037	0.0011

Table 4.3: Acceptance area for total number of counts for each individual subangle for LEH.
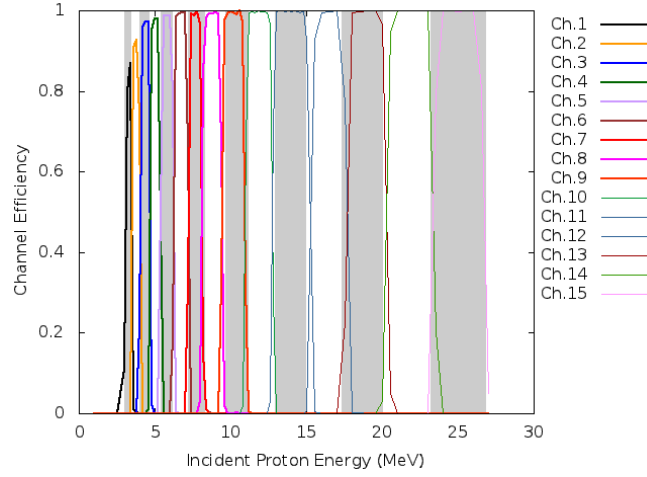
Figure 4.3: Energy bins for LEH and GEANT4 simulation of detector response function to particles on axis at 0^0 angle of incidence.

  (ii) Counts in the correct channel versus angle

(iii) Sum of counts in the wrong channels versus angle for each energy.

As stated earlier, the source makes an angle θ with the axis, thus the effective area of the source decreases as the incident angle of the source increases so the over lapping area of the disk source to the inner entrance hole decreases as shown in Fig. 3.18 which in turn will decrease the number of particles hitting the detector i.e. a decrease in number of counts. Thus the acceptance area of the disk source to the entrance cone decreases gradually with incident angle going from 0 to 12.5^0. Table 4.3 gives the acceptance area for each subangle from 0^0 to 12.5^0 for the all counts.
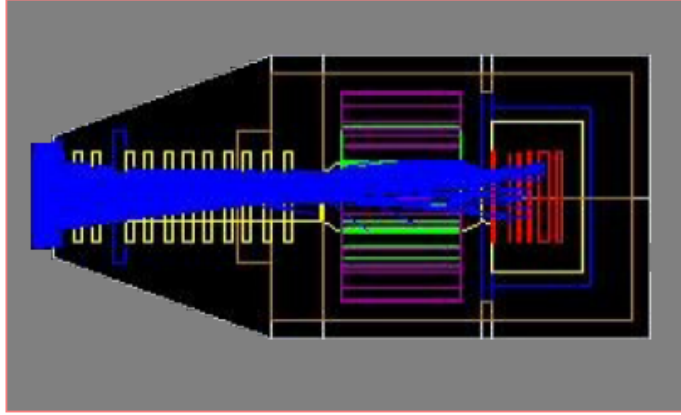
Figure 4.4: 1D beam source for calculating the geometric factor at an axial angle of 7.5^0 and fixed value of ϕ for LEH.

Angle	5 MeV	12 MeV	22.5 MeV
0^0- 2.5^0	0 .0015	0.00176	0.001846
2.5^0- 5^0	0.011	0.0118	0.012290
5^0- 7.5^0	0.0107	0.0117	0.011765
7.5^0- 10^0	0.0035	0.00336	0.003252
10^0 - 12.5^0	0.000124	0.0001	0.000176
12.5^0- 15^0	0	0.000035	0.000065

Table 4.4: Partial geometric factor cm^2srad for each sub angular range for the counts detected in all channels for LEH case

The partial geometrical factors for the all counts, the correct counts and the wrong counts for each angular range are listed in Tables 4.4, 4.5 and 4.6 for each angle respectively. The total geometrical factor for all, correct and wrong channel counts is calculated by summing up the partial geometric factors and is listed in Table 4.7. It is the sum of partial geometrical factors at each angle for a particular energy as listed in Tables 4.4, 4.5 and 4.6. One can see that at the highest energy the total geometric factor is close to that of an ideal two aperture source but that approximately 6% of the ideal value.

Angle	5 MeV	12 MeV	22.5 MeV
0^0- 2.5^0	0 .0015	0.00176	0.001839
2.5^0- 5^0	0.01062	0.0114	0.011574
5^0- 7.5^0	0.0105	0.0112	0.011216
7.5^0- 10^0	0.0034	0.0031	0.002966
10^0 - 12.5^0	0.0001	0.000005	0.000010
12.5^0-15^0	0.00	0.00	0.00

Table 4.5: Partial geometrical factor ($cm^2 srad$) for correct counts detected for LEH

Angle	5 MeV	12 MeV	22.5 MeV
0^0- 2.5^0	0.00	0.00	0.000005
2.5^0- 5^0	0.00038	0.0004	0.000477
5^0- 7.5^0	0.0002	0.0005	0.000525
7.5^0- 10^0	0.0004	0.00026	0.000286
10^0 - 12.5^0	0.000024	0.000095	0.000166
12.5^0-15^0	0.00	0.000035	0.000065

Table 4.6: Partial geometrical factor ($cm^2 srad$) for wrong counts detected for LEH

Energy	G_{total}	$G_{correct}$	G_{wrong}
5 MeV	0.0268±0.0001	0.0261±0.0001	0.0007±0.000
12 MeV	0.0288±0.0001	0.0275±0.0001	0.00129±0.000
22.5 MeV	0.0294±0.0001	0.0276±0.0001	0.0018 ±0.000

Table 4.7: Total geometric factor for the all, correct and wrong channels by adding the individual GF at each angle for LEH .
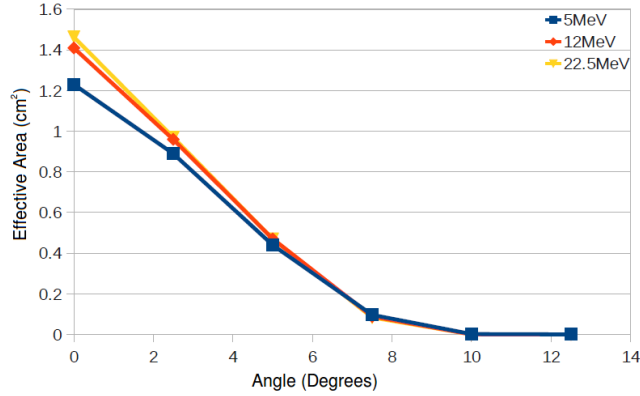
Figure 4.5: Effective area versus incident angle of the source

4.2.3 Geometric Factor by Taking Isotropic Source

For the second calculation of geometric factor another approach for the simulations with an isotropic source was employed to carry out the calculations. A full isotropic source is fairly inefficient for such calculations because most of the particles miss the detector. The source was made efficient by limiting the angle between 0 and θ_m which is possible for circularly and cylindrically symmetric source. For this purpose a circular disk source of radius 1.5 cm was defined to emit particles isotropically between 0^0 to 12.5^0 in a solid angle as calculated in equation (4.1). The sources emitting 100,000 particles at energies 5 MeV, 12 MeV and 22.5 MeV were used in the simulations. The particles deposited all or a fraction of energy they carried while passing through the array of detectors. The deposited energies were analysed and if they satisfied any of the entries in the logic table given in Table 4.2 they were considered as a count in a particular energy bin.

The source solid angle Ω_{src} and Flux per unti area per srad, F_Ω, are

$$\Omega_{src} = 0.1488 srad. \tag{4.1}$$

$$F_\Omega = 95120.96 cm^{-2} srad^{-1} \tag{4.2}$$

Figs. 4.6, 4.7 and 4.8 show the $A_{acceptance}$ calculated by equation (3.3)

Energy	C_{total}	$C_{correct}$	C_{wrong}
5 MeV	2533	2471	62
12 MeV	2672	2575	97
22.5 MeV	2764	2635	129

Table 4.8: Counts in all, correct and wrong channels for isotropic source with 12.5^0 halfwidth angle for LEH .

Energy	G_{total}	$G_{correct}$	G_{wrong}
5 MeV	0.0266±0.0005	0.0259±0.0005	0.0007±0.000
12 MeV	0.0281±0.0005	0.0271±0.0005	0.0010±0.00
22.5 MeV	0.0291±0.0006	0.0277±0.0005	0.0014±0.00

Table 4.9: Total Geometric Factor for the all, correct and wrong channels for isotropic source with 12.5^0 halfwidth angle for LEH.

for corresponding angle at 5 MeV, 12 MeV and 22.5 MeV for all, correct and wrong channel counts. Tables 4.8 and 4.9 list the number of counts and geometric factor for the all, the correct and the wrong channels for the isotropic source with 12.5^o halfwidth angle for HEH.

4.2.4 Discussion:

The results obtained from the three approaches in sections (4.2.1), (4.2.2) and (4.2.3) show that the values of geometrical factor are in good agreement with each other. If we compare the results of the two simulation approaches used in sections (4.2.2) and (4.2.3) with each other we can see that the values of G for the correct channels are in good agreement. At, 5 MeV with an error 0.75%, 12 MeV with an error of 1.5% and at 22.5 MeV with error about 1.0% which indicates agreement within the error bars of the calculations.

If we compare the two simulation aproaches with two aperture calculation it can be seen that at 5 MeV there is about 8% error between
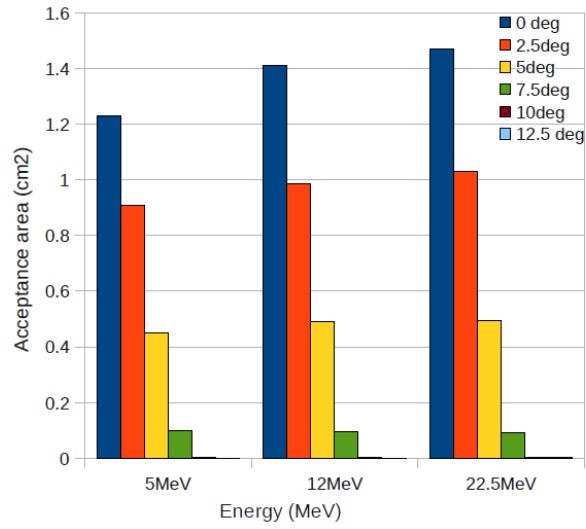
Figure 4.6: $A_{acceptance}$ for the counts detected in all channels vs angles for LEH case.
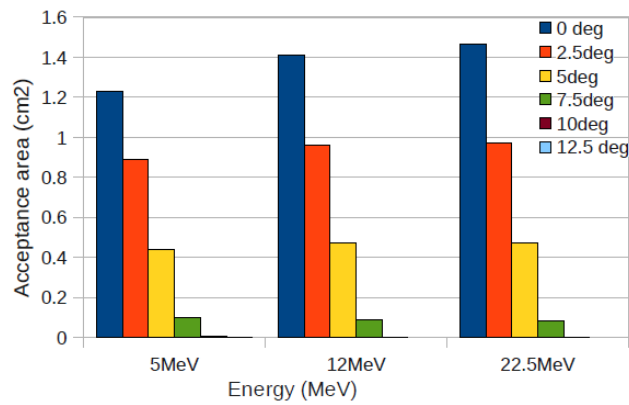
Figure 4.7: $A_{acceptance}$ for the counts detected in correct channels vs angles for LEH case.
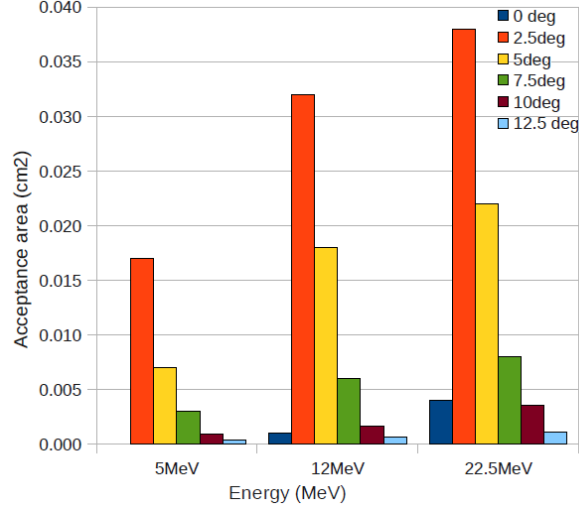
Figure 4.8: $A_{acceptance}$ for the counts detected in wrong channels vs angles for LEH case.

the three, at 12 MeV the error is reduced to 1% and at 22.5 MeV there is further decrease in error about 0.3%. Since at low energies the scattering can reduce the energy of the particle or deflect the particle out of the beam thus reduces the number of correctly calculated particles which in turn will reduce the value of G. If this deposited energy is less than the lower limit of the logic bin it may reduce the number of events detected. Thus reducing the value of G.

Also it is observed that the contribution from the incorrect counts to G is very small about 2.5 % for LEH case. This is because of the small acceptance angle of the cone angle for LEH which minimizes scattering into lower energy channels. Particles at an angle θ along the axis reduce their observed range by a factor of $cos\theta$. However, since only particles at small angles can enter through the entrance window thus the decrease in range is very small. For the present calculation we have taken the central energy of an energy bin e.g. 5 MeV, 12 MeV and 22.5 MeV, so that a small decrease in energy may not affect the particular binning energy range. Therefore, there is very small contribution to the incorrect channels in LEH case. A

more detailed calculation should take into account a weighted average of different energy particles in a given bin where those close to the bottom of the energy bin may have increased false counts. However, it is expected that this will be small correction factor to the above results.

4.3   Conclusion:

The observed value of geometrical factor is in good agreement with the theoretical value at low energies with an error of about 1.5% for LEH as currently configured. The incorrect counts can be reduced by decreasing the acceptance angle of the cone but the current level of accuracy is deemed acceptable for LEH design. Also the angular and energy dependent data describes the detector response function in detail and in the future could be used to correct raw measured data using iterative deconvolution routines.

Chapter 5

HEH Prototype

5.1 Prototype Tests

A prototype detector head was designed, fabricated and tested at TRI-UMF by Henry Tiedje in the Laser Plasma Research group. In this chapter detailed simulation modeling, experimental design of the prototype High Energy Head and results obtained from the experiments performed at the TRIUMF proton accelerator facility will be presented.

5.1.1 Design Modeling of Triumf prototype

A prototype detector design was proposed for the HEH with a reduced number of silicon detectors. In order to optimise the design, it was necessary to test the design using GEANT4 simulations. For this purpose a flexible layout using 4 silicon detectors and 3 degraders was proposed as shown in Fig.5.1. With this design any combination of detector elements in the HEH of the form D2, D3, Dx, Dy could be simulated in the prototype detector. The first degrader is 3.175 mm thick aluminum disk which is placed in front of the first two detector elements D2 and D3. Degraders 2 and 3 are placed between D4 and D5 respectively. The thickness of the first aluminum degrader is adjusted in such that it replaces spacer 1 and 2 and detector element D1 of the detailed HEH design.

The reduced design was congiured to work as D2D3D4D5, D2D3D6D7,
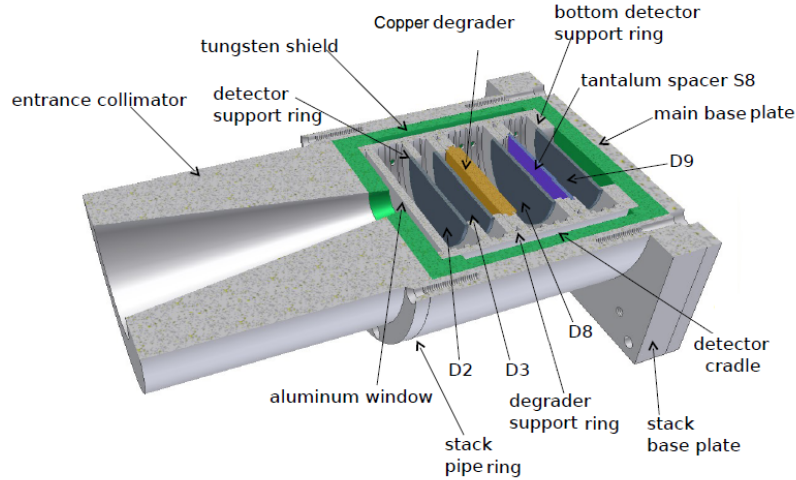
Figure 5.1: HEH prototype with four stack detector elements.

Degrader2 (*mm*)	Degrader3 (*mm*)	Configuration
Tantalium 0.127	Tantalium 0.254	D2D3D4D5
Tantalium 1.524	Tantalium 0.762	D2D3D6D7
Copper 5.895	Tantalium 1.499	D2D3D8D9
Copper 12.324	Tantalium 2.921	D2D3D10D11

Table 5.1: Degraders thickness and materials used to achieve proper configuration

D2D3D8D9 and D2D3D10D10 configurations by changing the thickness of the degraders 2 and 3. The thickness of degraders was adjusted by simulating the equivalent amount of energy deposited in each stack element detector and spacers of the detailed design for each configuration. For D2D3D4D5 and D2D3D6D7 configurations the degrader 2 was made of tantalium while to achieve D2D3D8D9 and D2D3D10D11 configurations copper was used in the degrader 2 material. Table 5.1 lists the thicknesses and the materials used for different configurations.

Working of TRIUMF Prototype

In order to check that the reduced design of the TRIUMF prototype performs similarly to that of the detailed HEH design of HEPT, simula-
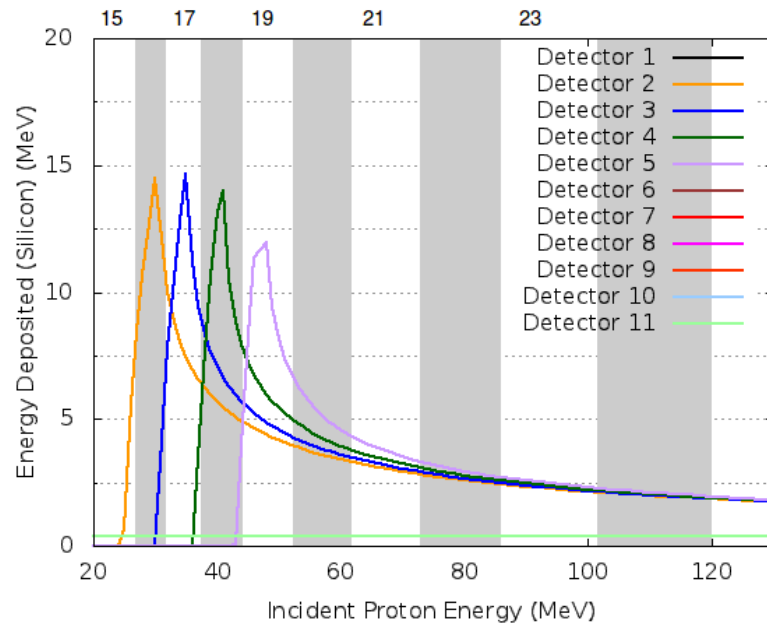
(a) Plot of energy deposited versus incident energy of proton for D2D3D4D5 configuration
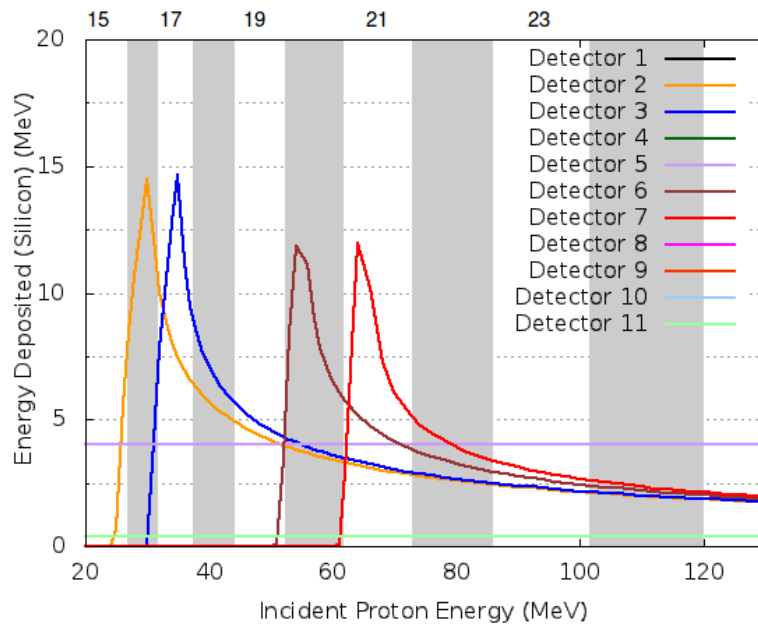
(b) Plot of energy deposited versus incident energy of proton for D2D3D6D7 configuration

Figure 5.2: Energy deposited versus incident energy in silicon Detector elements for (a) D2D3D4D5 and (b) D2D3D6D7 ,configurations.
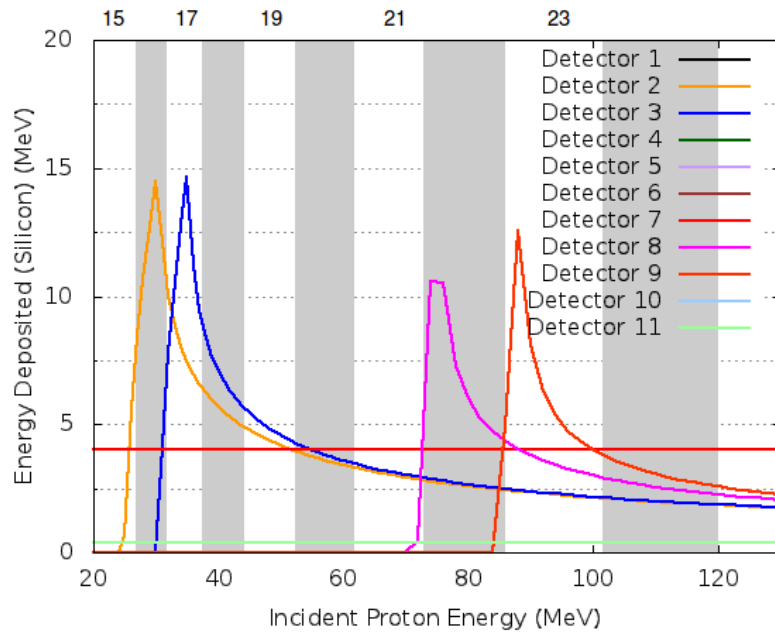
(a) Plot of energy deposited versus incident energy of proton for D2D3D8D9 configuration
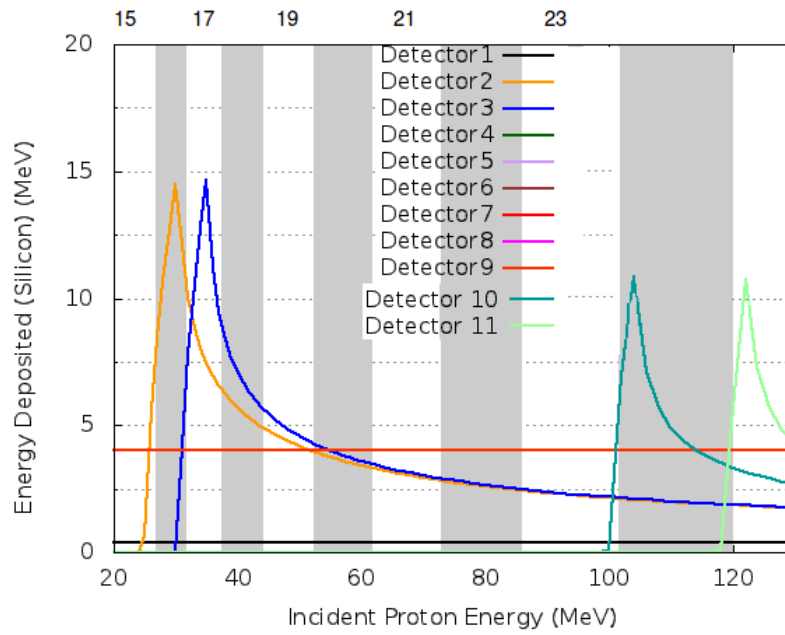
(b) Plot of energy deposited versus incident energy of proton for D2D3D10D11 configuration

Figure 5.3: Energy deposited versus incident energy in silicon Detector elements for (a) D2D3D8D9 and (b) D2D3D10D11 configurations.

tions were performed by making D2D3D4D5, D2D3D6D7, D2D3D8D9 and D2D3D10D11 configurations by changing the thickness and materials of degraders 2 and 3, as indicated in Table 5.1. Energy deposited vs incident Energy and the channel response function were plotted and compared with the detailed design. Figs. 5.2 and 5.3 show the energy deposited in the detectors for different configurations, used. Figs. 5.4 and 5.5 show the channel efficiency for all the configurations obtained by passing the signals through the same logic as for the case of HEH. It can be seen from the energy deposition and channel response function plots that the reduced design works very well and is similar to the detailed design of HEPT.

5.2 HEPT Experimental Design

The HEPT proof of principle sensor uses the same sensor elements as proposed for the final HEPT detector. Each silicon detector element is 1.5 mm thick and is installed on a space qualified mounting element. The four silicon detectors in the prototype HEH are mounted on aluminum support rings with nylon screws as shown in Fig.5.6. The support rings are held in grooves inside an aluminum cradle which is split into two halves. The annular grooves are machined at 0.4 inch intervals along the length of the cradle, so that detectors and degrader spacers Fig.5.6 are mounted at intervals along the axis of the detector stack. Each detector has a ribbon cable for connection to the detector amplifier printed circuit board (PCB). A channel for the ribbon cables is provided by a slot in one cradle half. The detector amplifier PCB is installed in an aluminum shielded box Fig.5.7 adjacent to the detector head mounted on the same main base plate. The ribbon cables terminate at connectors on the amplifier printed circuit board (PCB).

The detector stack is housed inside both aluminum and tungsten

93
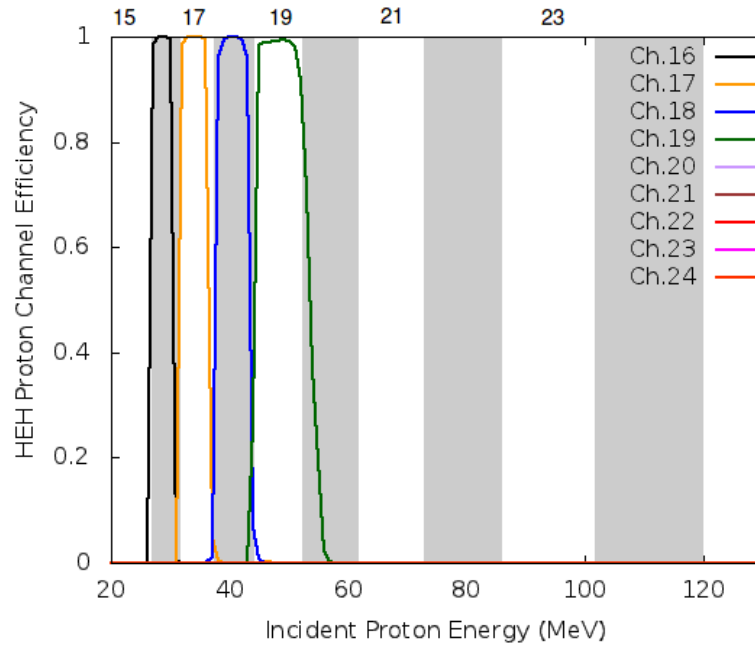
(a) Channel efficiency versus incident proton energy for D2D3D4D5
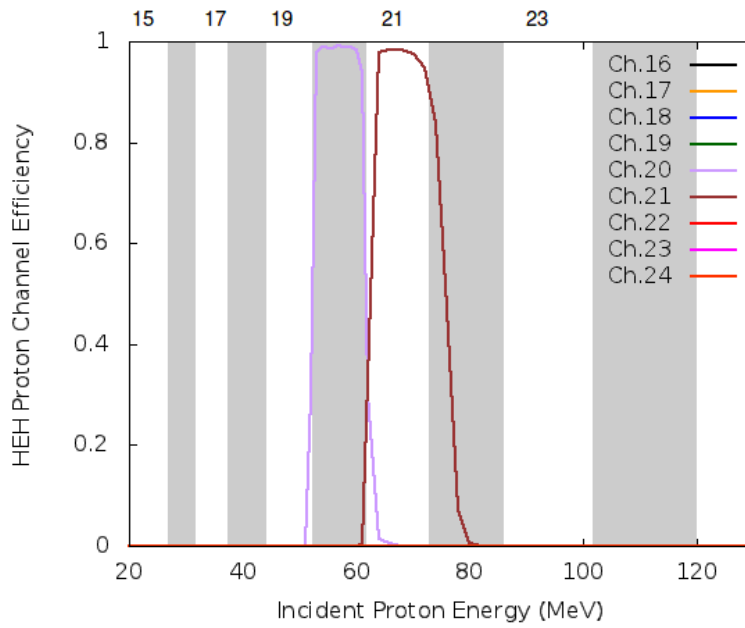
(b) Channel efficiency versus incident proton energy for D2D3D6D7

Figure 5.4: Channel efficiency versus incident energy for (a) D2D3D4D5 and (b) D2D3D6D7 configurations.
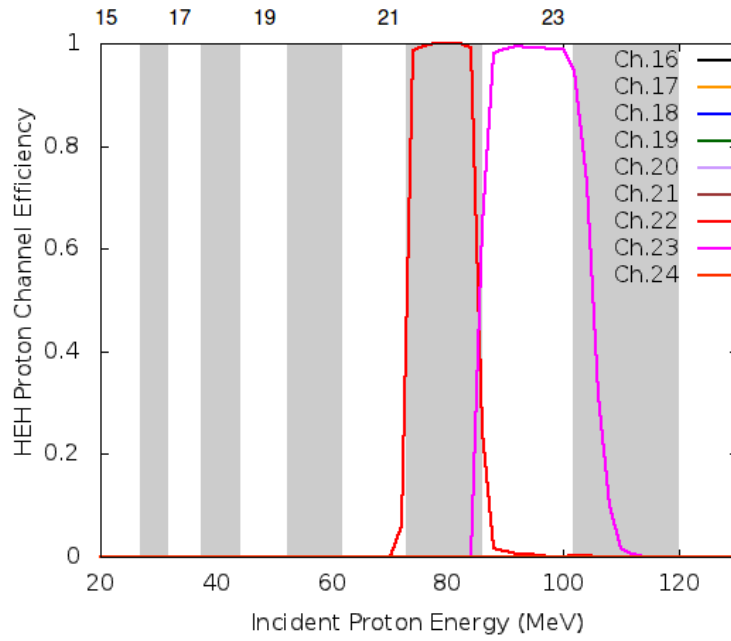
(a) Channel efficiency versus incident proton energy for D2D3D8D9
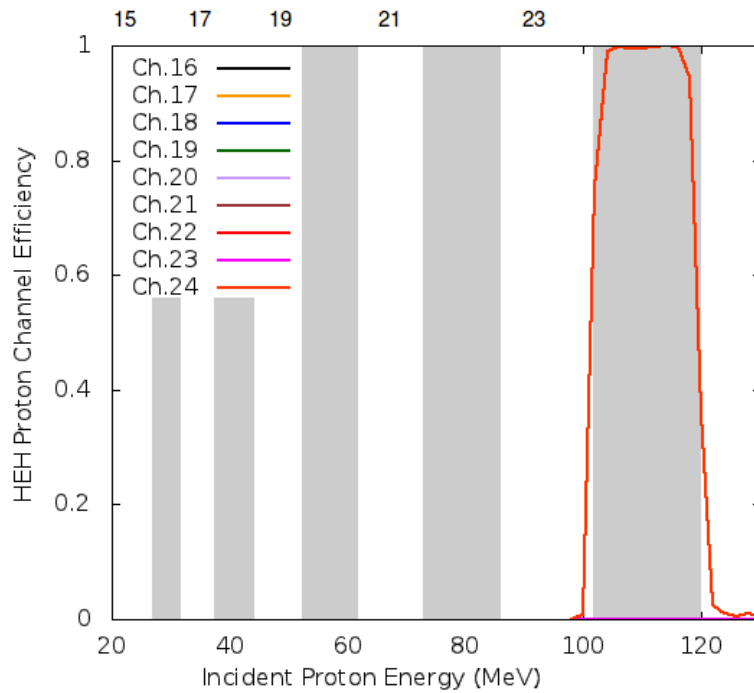
(b) Channel efficiency versus incident proton energy for D2D3D10D11

Figure 5.5: Channel efficiency versus incident energy for (a) D2D3D8D9 and (b) D2D3D10D11 configurations.
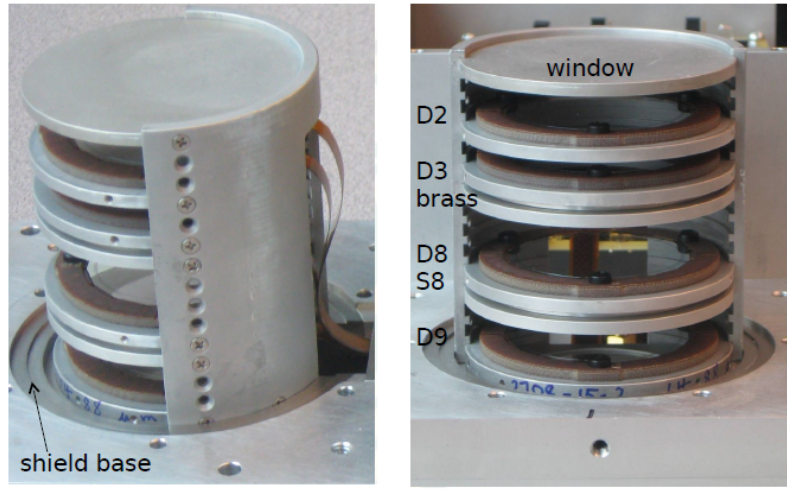
Figure 5.6: Figure shows aluminum support rings to mount silicon detectors and degraders
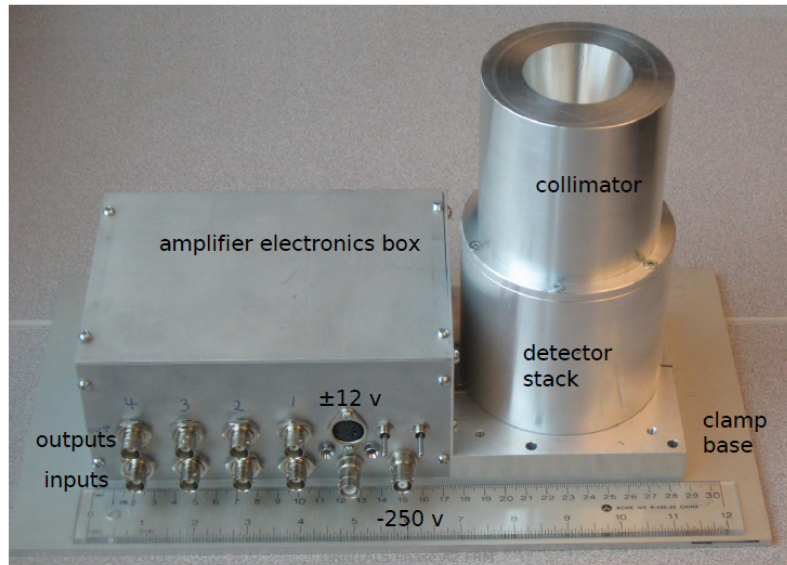
Figure 5.7: Front view of HEH prototype with reduced stack detector elements.

cylindrical shielding layers. The composition of the tungsten layer is 90% W, 6% Ni and 4% Cu by weight, the density is 17.12 g/cm^3 and the thickness is 7.62 mm. The tungsten layer is surrounded by an aluminum wall of thickness 7.556 mm. Inside the tungten layer is an inner aluminum wall which supports the silicon detector assemblies and has thickness of 3.81 mm. The shielding stops protons up to energies of 90 MeV. Since the maximum energy proton beam available at TRIUMF was 104 MeV, therefore, the shielding penetration energy was reduced slightly (90 MeV) to observe sidewall penetration of protons. The entrance cone of the detector was made of aluminum. The cone was designed to study the the effects of spurious events from particles hitting and scattering from the cone entrance aperture. Some of the spurious events were observed, however, most of these events do not trigger a correct set of detector responses and would not register as a valid energy particle count.

5.2.1   Beam line Arrangment for Experiment

Fig-5.8 shows the beamline set up used for experiment performed at the TRIUMF facility in Vancouver, BC. The prototype has been tested using a high energy proton source. The energy of the protons in the beam was taken as 116 MeV and 74 MeV, respectively for the two energies available at the facility. A variable thickness degrader plate called the range shifter was used to obtain the required test energies.

A GEANT4 model of the main proton beamline components and detector entrance cone is shown in Fig.5.9. For the simulation the beamline arrangement was simplified from the one used at TRIUMF beam facility, by excluding some of those components which contributed only a very small amount to the degradation or scattering so that can be neglected. By implementing detailed simulation model in GEANT4, detector response functions to the proposed proton measurement values have been modeled.
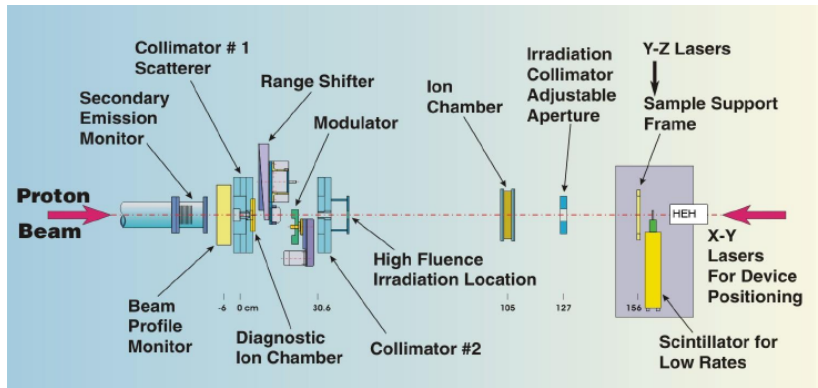
Figure 5.8: a beamline set up used for experiment performed at the TRIUMF facility
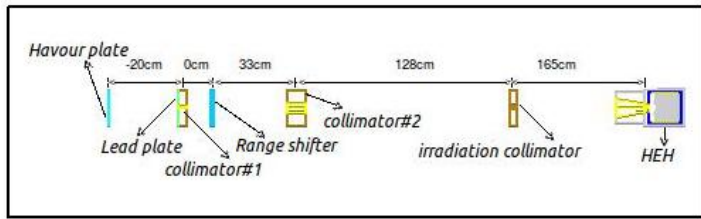
(a) A beamline set up modeled in Geant4 for simulations
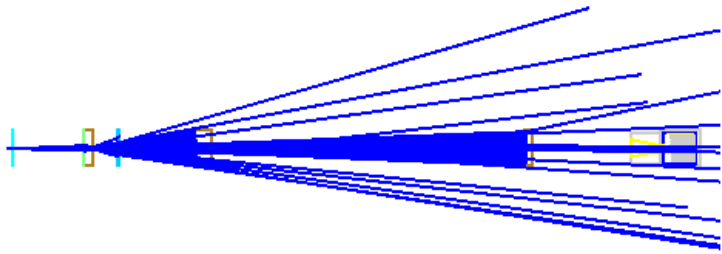
(b) Figure shows GEANT4 simulations of Triumf experimental set up. Simulations are shown for 100 protons at 74 MeV.

Figure 5.9: Beamline setup used for, (a) experiment and (b) simulations

Fig.5.9b shows the simulations of 100 protons at 74 MeV. It can be seen that most of the protons miss the detector, thus making the process some what inefficient. In order to obtain a statistically significant number of counts a source of 500,000 protons was used. Since a large number of protons are scattered at different directions due to all the degrader components, the number of counts was normalised by number of events that show energy > 0 at the first detector D2. For D2D3D8D9 configuration, the beam energy was 116 Mev, a copper plate of thickness 5.895 mm was used as degrader 2 and a tantalum plate of thickness 1.499 mm was used as degrader 3 for the experiment and simulations.

Figs.5.10(a) and 5.10(b) show the channel efficiency for D2D3D8D9 configuration versus incident energy of protons taken from the experimental data and simulations respectively. The efficiency of the detector is more than 65%. The incident flux is obtained by degrading the primary beam so it is no longer monoenergetic after passing through all the degraders. Some of the events are at low energy or large incident angle. After depositing some energy at D2 the particles might be scattered in different directions without depositing energy in the other detectors or they might not have enough energy to penetrate through the next degraders and detector elements. It can be seen that there is a slight discrepancy of the Ch 22 to Ch 23 transition point between experiment and simulation. This might be due to those beamline components which were not included in the simulations. Also the source distance from the front opening of the detector was taken about 2 m in the experiment which was reduced to 1cm in the simulations. It was done to get more statistics at the first detector. So the Transition point apearently has been shifted towards lower energy in the plot. It can also be seen that the particle with higher energies (90 - 100 MeV) are contributing into lower energy channel. As discussed earlier
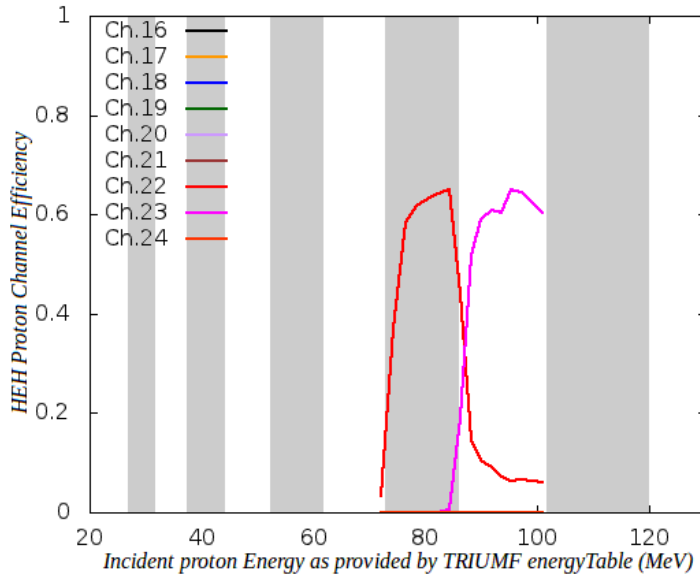
(a) Channel efficiency versus incident energy of proton for D2D3D8D9 configuration from experimental data
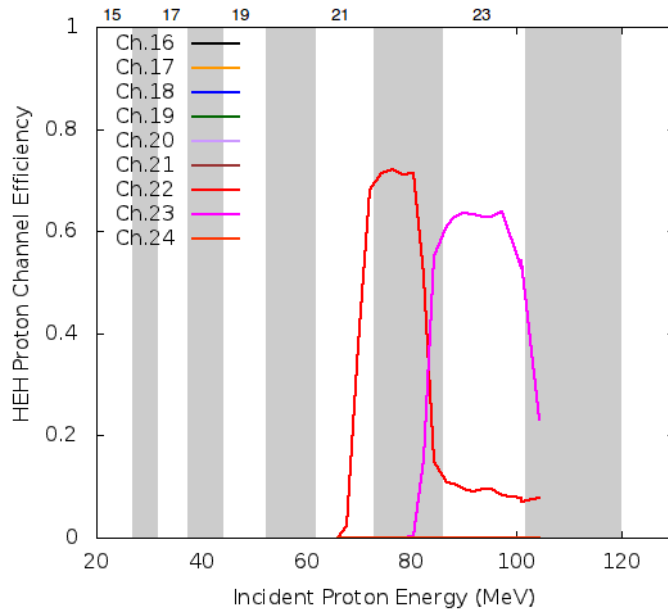
(b) Channel efficiency versus incident energy of proton for D2D3D8D9 configuration from simulations

Figure 5.10: Channel efficiency versus proton incident energy from, (a) experiment and (b) simulations.

the incident energy is a spread due to degradation and scattering so the particles do not deposit the exact energy required for a given channel and, in particular, angular deflections will tend to reduce the axial penetration and energy deposition profile which might satisfy the logic requirement for lower channels so that higher energy protons can contribute to lower energy channels as seen above. Also there might be nuclear interactions which may reduce the particle energy from its incident energy thus contributing in the lower energy channels. This is simulated at present with the physics package that includes nuclear interactions in the present GEANT4 simulations for HEH prototype.

5.3   Conclusion

The simulation model of the TRIUMF prototype is in reasonable agreement with the experimental measurements made when we take into account all the degraders and detector elements in the beam path.. In particular, the TRIUMF experimental results for D2D3D8D9 detector congurations, as shown in Figs.5.10(a) and 5.10(b), are in reasonable agreement with the GEANT4 simulations of the prototype HEH. Since the incident energy beam is not monoenergetic, due to the degraders and other beamline components, some spreading of the energy bins is observed. Also the scattering of particles at some angles off axis reduces the axial range and thus can lead to counts in lower energy channels. It is expected that nuclear interactions may also effect the detection of higher energy incident particles contributing to false counts in the lower channels and reducing the efficiency of the higher energy channels by an additional few percent which has not been included in the present calculations. However, the overall accuracy of the detector calibration appears to be in the range of several percent at present in terms of detector efficiency and energy bin edges.

Chapter 6

Conclusions

The HEPT is intented to measure the energetic electron and proton populations in the radiation belts. The performance of HEPT is enhanced from that of the previous such detector, PROTEL, by increasing the energy range and geometric factor of sensor heads and reducing the detector dead time. This results in an increase in dynamic range of energy and statistical accuracy of the detector.

By using aluminum spacers and discrete detector elements for each proton channel, a robust design of HEH is achieved which provides accurate detection of protons. The expected maximum count rate of 3000 counts per second based on AP8-MAX is well within the maximum count rate of 200,000 cps specification for our detector and allows 70 times dynamic range for magnetic storm events. In the same detector geometry electron detection can be achieved in five energy bins from 3 to 20 MeV using differential channels calculated from the actual detector channels. The maximum detection rate based on the worst case is of the order of 34,000 cps in the first signal detector which is still within the maximum counting rate of 200,000 cps specification for our detector.

The count rate of spurious events due to penetration of energetic particles from the side is very low due to the thick wall shielding. The shielding will block protons below 72 MeV and electrons below 8 MeV.

Furthermore the angular coincidence requirement reduces the effects of spurious events greatly because these spurious events would also have to simultaneously trigger all the intermediate detector elements in order to be counted as a real event.

The LEH has a smaller entrance cone angle than the HEH. Thus the particles at higher angle can not enter the detector due to smaller FOV of the detector. The value of geometrical factor obtained from simulations is in good agreement with the theoretical value at low energies with an error of about 1 to 5% for LE H as currently configured. The incorrect counts could be reduced by decreasing the acceptance angle of the cone but the correct level of accuracy is deemed acceptable for LEH design. Also the angular and energy dependent data describes the detector response function in detail and in the future could be used to correct raw measured data using iterative deconvolution routines.

The HEH has a larger entrance cone angle thus allowing particles comming in at larger angles. However, the particles incident at larger angles show up as lower energy from their incident energy which contributes to incorrect counting in the energy channels. The value of geometrical factor observed by simulations is in good agreement with the theoretical value at low energies but at high energies the total geometric factor is considerably lower for the HEH as currently configured. This is because, at high energies, the particles incident at some angle will reach the end of their penetration range at a shorter axial distance and not reach the particular end range detector for their particular energy bin, thus contributing to the lower energy channel counts. Usually the particles with energies close to the lower limit of bin range contribute to the incorrect counts. Th e scattering by the walls of entrance cone and detector shielding and penetration through the edges of entrance window are the other reasons which contribute to

the false counts. The incorrect counts can be reduced by decreasing the acceptance angle of the entrance cone. The angular and energy dependent data describes the detector response function in detail and in the future could be used to correct raw measured data using iterative deconvolution routines. However it appears that the large acceptance angle of the current HEH design leads to many wrong counts at larger entrance angles and thus these larger angles are not contributing effectively to the signal. In this case, future improvements should probably choose a somewhat smaller entrance cone angle for the HEH.

The simulation model of the TRIUMF prototype is in reasonable agreement with the experimental measurements made when we take into account all the degraders and detector elements in the beam path. In particular, the TRIUMF experimental results for D2D3D8D9 detector configuration, as shown in Figs.10a and 10b, are in reasonable agreement with the GEANT4 simulations of the prototype HEH. Since the incident energy beam is not monoenergetic, due to the degraders and other beamline components, some spreading of the energy bins is observed. Also the scattering of particles at some angles off axis reduces the axial range and thus can lead to counts in lower energy channels. It is expected that nuclear interactions may also effect the detection of higher energy incident particles contributing to false counts in the lower channels and reducing the efficiency of the higher energy channels by an additional few percent which has not been included in the present calculations. However, the overall accuracy of the detector calibration appears to be in the range of several percent at present in terms of detector efficiency and energy bin edges.

In the future, the energy range coverage of the detector could be increased to a few hundred MeV to study the behaviour of even higher energy protons in the radiation belts. If the current dE/dx type design is

used, this would require the use of fairly thick degraders of high-Z material such as tantalum, as already considered here. This would add considerable weight to the detector but has the advantage of a robust design primarily based on particle penetration range. It is estimated that an upper energy limit of 300 to 400 MeV could be achieved with such a design. At the same time modeling including nuclear interactions would be required in order to characterize the detector response in this higher energy range. To achieve even higher energy detection, alternative detection techniques such as Cerenkov emission could be employed to extend the detection capabilities to the GeV range.

It has been shown that the large entrance cone angle of the HEH contributes to a large number of incorrect counts (about 48%) which reduces the channel efficiency. By making the entrance cone angle smaller the incorrect counts can be reduced and hence the channel efficiency can be enhanced. A study should be carried out to identify an optimum collection cone angle for the HEH. The interference of high energy electrons with low energy protons can also result in a false estimation of channel efficiency. A study should be carried out to study this effect in greater detail, though such multiple particle sources are not very easy to implement in GEANT4 and would probably require a special source routine to be written.

The coincidence requirement of the HEH and the entrance cone angle reduces the probability of spurious counts from the side considerably. Thus, it might be possible to make the side wall shielding thinner which would reduce the weight of the detector. This is another aspect which could be studied in more detail. The current study has been able to characterize, via numerical simulations, the response of the proposed HEPT detector to an accuracy of the order of a few percent in energy response, geometric factors and channel efficiency for the detection of MeV protons and has given

an initial characterization of the response to MeV electrons. With these results and the numerical simulation techniques demonstrated, it should be possible to develop and characterize optimum high energy particle telescopes to meet the requirements of any future Canadian space missions.

Bibliography

[1] R. Fedosejevs. University of Alberta, Canada, Laser Plasma Research Group, Electrical and Computer Engineering, 2004.

[2] "http://www.spenvis.oma.be/help/background/traprad,"

[3] M. K. Hudson, B. T. Kress, H.-R. Mueller, J. A. Zastrow, and J. B. Blake, "Relationship of the Van Allen Radiation Belts to Solar Wind Drivers," Journal of Atmospheric and Solar-Terrestrial Physics, vol. 70, no. 5, pp. 708 – 729, 2008.

[4] J. Cummings, A. Cummings, R. Mewaldt, et al., "SAMPEX Measurements of Heavy Ions Trapped in the Magnetosphere," Nuclear Science, IEEE Transactions on, vol. 40, pp. 1458 –1462, dec 1993.

[5] D. M. Sawyer and J. I. Vette, "AP-8 Trapped Proton Environment for Solar Maximum and Solar MinimumAP-8 Trapped Proton Environment for Solar Maximum and Solar Minimum," NSSDC/WDC-A-R & S 76-06,, 1976.

[6] J. I. Vette, "The AE-8 Trapped Electron Model Environment," NSSDC/WDC-A-R & S 91-24, 1991.

[7] M. Cyamukungu, J. B. Blake, G. Grégoire, et al., "Proton Spectra Detected by the Proton Switches on the CRRES Satellite," Journal of Spacecraft and Rockets, vol. 38, pp. 584–589, July 2001.

[8] I. R. Mann, S. Beaudette, L. G. Ozeke, et al., "The Outer Radiation Belt Injection, Transport, Acceleration and Loss Satellite (ORBITALS): A Proposed Canadian Small Satellite Mission for ILWS.," AIP Conference Proceedings, vol. 1144, no. 1, pp. 146 – 156, 2009.

[9] J. Sullivan, "Geometric Factor and Directional Response of Single and Multi-element Particle Telescopes," Nuclear Instruments and Methods, vol. 95, no. 1, pp. 5 – 11, 1971.

[10] J. Fennell, H. Koons, M. Chen, and J. Blake, "Internal Charging: A Preliminary Environmental Specification for Satellites," Plasma Science, IEEE Transactions on, vol. 28, pp. 2029 –2036, dec 2000.

[11] L. Tverskaya, "Dynamics of the Earths Radiation Belts," Moscow University Physics Bulletin, vol. 65, pp. 246–251, 2010. 10.3103/S0027134910040028.

[12] S. Bourdarie and M. Xapsos, "The Near-Earth Space Radiation Environment," Nuclear Science, IEEE Transactions on, vol. 55, pp. 1810 –1832, aug. 2008.

[13] L. I. Miroshnichenko, Radiation Hazard in Space. KLUWER ACADEMIC PUBLISHERS Dordrecht Boston, 2003.

[14] L. A. Fisk, B. Kozlovsky, and R. Ramaty, "An Interpretation of the Observed Oxygen and Nitrogen Enhancements in Low-Energy Cosmic Rays," apjl, vol. 190, p. L35, May 1974.

[15] C. E. McIlwain, "Coordinates for Mapping the Distribution of Magnetically Trapped Particles," jgr, vol. 66, pp. 3681–3691, Nov. 1961.

[16] B. Rossi, Cosmic Rays. New York: McGraw-Hill, 1964.

[17] G. Withbroe, M. Guhathakurta, and J. Hoeksema, "Origins of the International Living With a Star program," Advances in Space Research, vol. 35, no. 1, pp. 40 – 3, 2005//. International Living With a Star program;organizational structure;international cooperative program;solar-terrestrial physics;.

[18] M. H. Johnson and J. Kierein, "Combined Release and Radiation Effects Satellite (CRRES) - Spacecraft and Mission," Journal of Spacecraft and Rockets, vol. 29, pp. 556–563, Aug. 1992.

[19] G. D. Reeves, "Radiation Belt Storm Probes: A New Mission for Space Weather Forecasting," Space Weather, vol. 5, pp. S11002–, Nov. 2007.

[20] D. Baker, "Solar Wind-Magnetosphere Drivers of Space Weather," Journal of Atmospheric and Terrestrial Physics, vol. 58, no. 14, pp. 1509 – 1526, 1996. Invited Review Articles from the 1995 CEDAR Workshop.

[21] M. Gussenhoven, E. Mullen, and D. Brautigam, "Near-earth Radiation Model Deficiencies as seen on CRRES," Advances in Space Research, vol. 14, no. 10, pp. 927 – 941, 1994.

[22] X. Li, D. N. Baker, S. G. Kanekal, M. Looper, and M. Temerin, "Long Term Measurements of Radiation Belts by SAMPEX and their Variations," Geophys. Res. Lett., vol. 28, no. 20, pp. 3827–3830, 2001.

[23] M. Gussenhoven, E. Mullen, and D. Brautigam, "Improved Understanding of the Earth's Radiation Belts from the CRRES Satellite," Nuclear Science, IEEE Transactions on, vol. 43, pp. 353 –368, apr 1996.

[24] G. Mason, D. Baker, J. Blake, et al., "SAMPEX: NASA's first Small Explorer Satellite," in Aerospace Conference, 1998 IEEE, vol. 5, pp. 389 –412 vol.5, mar 1998.

[25] R. Hoffman, "PolarFrom the Top Down," Advances in Space Research, vol. 20, no. 45, pp. 569 – 573, 1997. Results of the IASTP Program.

[26] G. D. Reeves, K. L. McAdams, R. H. W. Friedel, and T. P. O'Brien, "Acceleration and Loss of Relativistic Electrons During Geomagnetic Storms," Geophys. Res. Lett., vol. 30, pp. 1529–, May 2003.

[27] M. Violet, K. Lynch, R. Redus, et al., "Proton Telescope (PROTEL) on the CRRES Spacecraft," Nuclear Science, IEEE Transactions on, vol. 40, pp. 242 –245, apr 1993.

[28] C. Lippmann, "Particle Identification," Nuclear Instruments and Methods in Physics Research Section A: Accelerators, Spectrometers, Detectors and Associated Equipment, vol. 666, no. 0, pp. 148 – 172, 2012. Advanced Instrumentation.

[29] J. F. Ziegler, "Stopping of Energetic Light Ions in Elemental Matter," Journal of Applied Physics, vol. 85, no. 3, p. 1249, 1999.

[30] J. F. Janni, "Energy loss, Range, Path length, Time-of-flight, Straggling, Multiple Scattering, and Nuclear Interaction Probability: In two parts. Part 1. For 63 compounds Part 2. For elements 1 Z 92," Atomic Data and Nuclear Data Tables, vol. 27, no. 23, pp. 147 – 339, 1982.

[31] S. Agostinelli, J. Allison, K. Amako, et al., "GEANT4 - A Simulation Toolkit," Nuclear Instruments and Methods in Physics Research Section A: Accelerators, Spectrometers, Detectors and Associated Equipment, vol. 506, no. 3, pp. 250 – 303, 2003.

[32] "GEANT - Detector Description and Simulation Tool, CERN Program Library Long Write-up W5013,CERN Geneva,"

[33] H. Chen, W. Shi, H. Zou, and J. Zou, "Discussion on the Geometric factor in the Detection of high Energy Electrons in Geospace," Science in China Series E: Technological Sciences, vol. 51, pp. 1–9, 2008. 10.1007/s11431-008-0002-3.

[34] "www.NIST.org,"